



AMERICAN METEOROLOGICAL SOCIETY

Journal of Climate

EARLY ONLINE RELEASE

This is a preliminary PDF of the author-produced manuscript that has been peer-reviewed and accepted for publication. Since it is being posted so soon after acceptance, it has not yet been copyedited, formatted, or processed by AMS Publications. This preliminary version of the manuscript may be downloaded, distributed, and cited, but please be aware that there will be visual differences and possibly some content differences between this version and the final published version.

The DOI for this manuscript is doi: 10.1175/JCLI-D-17-0670.1

The final published version of this manuscript will replace the preliminary version at the above DOI once it is available.

If you would like to cite this EOR in a separate work, please use the following full citation:

Ciesielski, P., R. Johnson, W. Schubert, and J. Ruppert, 2018: Diurnal Cycle of the ITCZ in DYNAMO. *J. Climate*. doi:10.1175/JCLI-D-17-0670.1, in press.

© 2018 American Meteorological Society



1
2
3
4
5
6
7
8
9
10
11
12
13
14
15
16
17
18
19
20
21
22
23

Diurnal Cycle of the ITCZ in DYNAMO

Paul E. Ciesielski*, Richard H. Johnson, Wayne H. Schubert

Department of Atmospheric Science,

Colorado State University,

Fort Collins, Colorado

James H. Ruppert Jr.

Max Planck Institute for Meteorology

Hamburg, Germany

Submitted October 2017

Revised February 2018

Submitted to the Journal of Climate

*Corresponding author address: Paul E. Ciesielski, Department of Atmospheric

Science, 1371 Campus Delivery, Colorado State University, Fort Collins, CO 80523

Email: paulc@atmos.colostate.edu

25 **Abstract**

26 During the 2011 special observing period of the Dynamics of the Madden-
27 Julian Oscillation (DYNAMO; MJO) field experiment, two sounding arrays were
28 established over the central Indian Ocean, one north and one south of the equator,
29 referred to here as the NSA and SSA, respectively. Three-hourly soundings from
30 these arrays augmented by observations of radiation and rainfall are used to
31 investigate the diurnal cycle of ITCZ convection during the MJO suppressed phase.
32 During the first half of October when convection was suppressed over the NSA but
33 prominent over the SSA, the circulation over the sounding arrays could be
34 characterized as a local Hadley cell. Strong rising motion was present within the
35 ITCZ extending across the SSA with compensating subsidence over the NSA. A
36 prominent diurnal pulsing of this cell was observed, impacting conditions on both
37 sides of the equator, with the cell running strongest in the early morning hours (05-
38 08 LT) and notably weakening later in the day (17-20LT). The declining daytime
39 subsidence over the NSA may have assisted the moistening of the low to mid-
40 troposphere there during the pre-onset stage of the MJO. Apparent heating Q_1 within
41 the ITCZ exhibited a diurnal evolution from early morning bottom-heavy profiles to
42 weaker daytime top-heavy profiles, indicating a progression from convective to
43 stratiform precipitation. Making use of the weak temperature gradient
44 approximation, results suggest that both horizontal radiative heating gradients and
45 direct cloud radiative forcing have an important influence on diurnal variations of
46 vertical motion and convection within the ITCZ.

47

48 **1. Introduction**

49 The diurnal cycle is a fundamental mode of the circulation and precipitation
50 variability in the tropics. While its characteristics and governing mechanisms over
51 land and coastal regions have been extensively studied and are well understood, the
52 same cannot be said for over the open ocean where the paucity of observations have
53 limited our ability to fully describe and understand it. Making creative use of surface
54 observations (e.g., COADS, buoy, and scatterometer winds), several studies have
55 examined its structure over the tropical oceans on seasonal to annual time scales
56 (e.g., Deser and Smith 1998; Dai and Deser 1999; Gille et al. 2003). A consistent
57 pattern has emerged from these studies, in which surface divergence in regions of
58 large-scale subsidence is a maximum (minimum) in the morning (evening) hours.
59 This diurnally varying circulation is compatible with an early-morning rainfall
60 maximum in adjacent regions of deep convection and associated overturning
61 circulation in response to cloud-radiative feedbacks (Gray and Jacobson 1977;
62 Randall et al. 1991). Yet, due to a lack of in situ observations, very few studies have
63 examined the modulation of large-scale overturning circulation by diurnally varying
64 organized deep convection. This study addresses this gap.

65 Nicholls (2015) gives a detailed review of the three main proposed mechanisms
66 by which radiation affects organized oceanic convective systems. The
67 “convergence/differential radiation” mechanism was originally proposed by Gray
68 and Jacobson (1977, hereafter GJ77), based on their observation that rainfall in
69 oceanic deep tropical convection is 2-3 times heavier in the early morning hours
70 than in the late afternoon and evening. This mechanism operates as follows: at night

71 radiative cooling is strong in the clear environment adjacent to regions of disturbed
72 weather, where smaller net cooling occurs; this results in enhanced subsidence in
73 the clear region and low-level convergence into convective regions; and during the
74 day, differential heating between clear and cloudy areas is reduced, leading to
75 weaker convection. A second mechanism, based on the modeling work of Dudhia
76 (1989) and Tao et al. (1996), emphasizes the role of large-scale radiative cooling in
77 increasing rainfall by raising the environmental relative humidity. The third
78 mechanism is referred to as “direct radiative-convective interaction,” or simply, the
79 lapse-rate mechanism (Kraus 1963; Randall et al. 1991, Xu and Randall 1994).
80 According to this mechanism, the absorption of shortwave radiation preferentially
81 near cloud top stabilizes the column, in turn suppressing convection during the
82 daytime, while longwave cooling from cloud tops acting alone at night leads to
83 increased lapse rates and rainfall.

84 Several past studies have explored the diurnal cycle of vertical motion and
85 convection over the open oceans using field campaign upper-air datasets. These
86 studies, spanning a broad spectrum of geographical locations and convective
87 regimes, are briefly summarized in Table 1¹. The diurnal characteristics of the
88 diagnosed fields vary greatly among the various regions. For example, within the
89 western Atlantic trade wind regime Nitta and Esbensen (1974) found that during a
90 undisturbed period in BOMEX the subsidence field, which peaked near the trade-
91 wind inversion top (~ 800 hPa), had a diurnal amplitude of ~ 2 hPa/h with a

¹ Experiment acronyms are listed in the Table 1 caption.

92 subsidence maximum (minimum) at 08 LT (20 LT). A smaller diurnal amplitude
93 (~ 0.8 hPa/h) was observed in the stratocumulus transition zone of ASTEX with
94 peak subsidence at 22 LT being nearly out of phase with that found in BOMEX
95 (Ciesielski et al. 2001). On the other hand, the deep convective environment of GATE
96 showed an afternoon convective maximum (Albright et al. 1981), while in TOGA
97 COARE the diurnal peak in convection varied depending on the convective regime
98 (Chen and Houze 1997; Sui et al. 1997) with an afternoon peak in suppressed
99 conditions and a late night to early morning peak in disturbed periods. Collectively,
100 these studies reveal a spatial complexity to the diurnal cycle and suggest a variety of
101 processes that influence it.

102 Observational studies of Inter-Tropical Convergence Zone (ITCZ) convection
103 over the oceans have generally used satellite data and reanalysis products to
104 characterize its behavior. For example, Waliser and Gautier (1993) used two
105 decades of global infrared and visible satellite products to document the seasonal,
106 annual, and interannual variability of the ITCZ. Using 23 years of European Centre
107 for Medium-Range Weather Forecasts (ECMWF) reanalyses, Magnusdottir and
108 Wang (2008) examined the synoptic scale variability of vorticity within several ITCZ
109 regions and found that their composite structure over the eastern and central
110 Pacific builds westward and tilts cyclonically in the latitudinal direction with time.
111 Employing a statistical method that objectively diagnoses regions of organized ITCZ
112 convection over the eastern Pacific using 3-h satellite data, Bain et al. (2010, 2011)
113 found a diurnal pulsing in the extent of the ITCZ cloud envelope with a 15%
114 afternoon increase along with a 13-16 LT minimum in IR temperatures. The results

115 presented in the current paper are intended to complement these earlier studies by
116 offering a unique perspective on the diurnal cycle of the ITCZ through use of 3-
117 hourly *in situ* sounding observations.

118 To investigate the mechanisms responsible for the initiation of the Madden-
119 Julian Oscillation (MJO, Madden and Julian 1972) over the Indian Ocean (IO), the
120 Dynamics of the MJO (DYNAMO) experiment was conducted during the period from
121 October 2011 to March 2012 (Yoneyama et al. 2013, Zhang et al. 2013). One of the
122 unexpected findings from DYNAMO was that ITCZ convection was present over the
123 Southern Hemisphere IO during the pre-onset (or suppressed) stage leading up to
124 both the October and November MJO events, and then shifted northward to the
125 equator during the MJO convectively active phases (Johnson and Ciesielski 2013;
126 Yoneyama et al. 2013; Kerns and Chen 2014). Later studies have shown that ITCZ
127 convection in the IO region is quite common. Using TRMM rainfall products over the
128 16-yr period from 1998-2013, Sodowsky (2016) and Zhang and Sodowsky (2016)
129 identified 205 ITCZ events lasting 2 days or longer over the IO region (60° - 90°E)
130 and 99 MJOs. These studies showed that the majority of these MJOs (~55%)
131 initiated within 2 weeks of a preceding IO ITCZ. These investigators hypothesized
132 that the ITCZ can serve as a major moisture source for subsequent MJO.

133 Ruppert and Johnson (2015) used high-time-frequency sounding and radar
134 measurements from DYNAMO to describe the diurnal cycle of shallow convection
135 during the suppressed phase of the MJO. They found that daytime convective-cloud
136 deepening and moistening of the lower troposphere was promoted by a
137 combination of daytime increased sea surface temperature (SST) and reduced large-

138 scale subsidence. The importance of such upper-ocean “diurnal warm layers” for
139 invigorating convection has also been noted by others (Chen and Houze 1997; Sui et
140 al. 1997; Johnson et al. 2001; Bellenger et al. 2010; Johnson and Ciesielski 2017).
141 Ruppert and Johnson (2016) conducted large-eddy simulations of this regime to
142 investigate the specific influences of diurnal changes in SST and large-scale
143 subsidence, wherein they parameterized subsidence using the weak temperature
144 gradient (WTG) scheme of Herman and Raymond (2014). Through similar
145 simulations, Ruppert (2016) found that this diurnal cycle of shallow convection
146 drives greater daily-mean precipitation, convective heating, and rising motion than
147 would otherwise occur, in turn accelerating the local onset of deep convection.
148 Given the potential importance of such a diurnal time-scale feedback, there is an
149 imperative to resolve the driving mechanism(s) for diurnal changes in large-scale
150 vertical motion. The hypothesis of Ruppert and Johnson (2015, 2016) that this
151 diurnal cycle was remotely forced by the ITCZ will be tested herein.

152 A significant component of the DYNAMO observational network involved an
153 enhanced network of upper-air sounding sites over the central IO (Fig. 1) composed
154 of two quadrilateral arrays – one north and one south of the equator – referred to as
155 the northern and southern sounding arrays or NSA and SSA. During the special
156 observing period (SOP) of the experiment (1 Oct – 30 Nov. 2011) these sites took 4
157 to 8 soundings per day. In this study we make use of this dataset to investigate the
158 diurnal cycle of convection during the suppressed phase of the October MJO in
159 which ITCZ convection was located across the SSA. This paper is organized as
160 follows: Section 2 describes the data products used in this study; Section 3 focuses

161 on the mean and diurnal characteristics of convection and the attendant flow field
162 during this period; Section 4 explores radiative and convective influences on the
163 ITCZ circulation; and Section 5 summarizes the results.

164 **2. Data and Analysis Procedures**

165 Gridded analyses of large-scale fields were used on a 1° grid with 25 hPa vertical
166 and 3-h temporal resolution covering the domain 20°N-20°S, 35°E -155°E. These
167 fields, constructed using multiquadric objective analyses (Nuss and Titley 1994) are
168 referred to here as the CSU V3b gridded product. Input to these analyses came
169 primarily from quality-controlled, bias-corrected, high vertical-resolution sounding
170 data (Ciesielski et al. 2014a). A procedure was developed to mitigate heat island
171 and flow blocking effects on Colombo sounding data (Ciesielski et al. 2014b) due to
172 the mountainous terrain of Sri Lanka. While sites in the SSA took 3-hourly
173 soundings during the SOP (Fig. 1), the Malé and Colombo sites generally had
174 soundings every 6 hours (at 00, 06, 12, and 1800 UTC). To generate a 3-hourly
175 frequency at these latter sites, i.e., to create pseudo soundings at 03, 09, 15, and 21
176 UTC, a linear interpolation was made between the 6-hourly soundings. To test the
177 accuracy of this approach, the same procedure was carried out at Gan where 3-
178 hourly soundings were actually taken. Comparison of interpolated soundings with
179 actual soundings indicates an estimated uncertainty of the time-interpolated fields
180 of 0.5°C, 0.5 g kg⁻¹ and 1 m s⁻¹ for temperature, specific humidity and wind speed,
181 respectively. In creating the gridded analysis product, the sounding data were
182 supplemented with satellite-derived winds, scatterometer surface winds, and radio-
183 occultation derived thermodynamic fields. ECMWF operational analyses (OA) were

184 used to augment the objective analyses in the large data void regions outside the
185 core sounding array and when the *Revelle* and *Mirai* research vessels were offsite.
186 However, for the regions and periods considered in this study, the ECMWF OA had
187 little, if any, impact on the analyses within the sounding arrays. The ECMWF OA
188 were also used for analysis of the velocity potential field, which covered a domain
189 larger than the CSU V3b product. Additional details on the supplementary data
190 sources mentioned above can be found in Johnson et al. (2015).

191 Other datasets used in this study include column-averaged (surface to 200 hPa)
192 all-sky radiation estimates provided by the Clouds and the Earth's Radiant Energy
193 System (CERES) product at 3-h resolution on a 1° grid (Wielicki et al. 1996).
194 Vertical profiles of longwave and shortwave heating rates over Gan Island (Fig. 1)
195 for both clear and all-sky conditions were obtained from the Pacific Northwest
196 National Lab (PNNL) Combined Retrieval (CombRet) product (Feng et al. 2014).
197 Combining the all-sky and clear retrievals gives us an estimate of the cloud-radiative
198 forcing (CRF). Satellite-estimated rainfall data were from the TRMM 3B42 V7
199 product at 0.25°, 3-h resolution (Huffman et al. 2007). Radar rainfall data from the
200 *Mirai*, *Revelle* and Gan-SPOL at 10-min resolution covering a 320 x 320 km domain
201 at each site were obtained from the DYNAMO legacy data archive and averaged into
202 3-hourly bins to facilitate comparison with other datasets at this temporal
203 resolution. In addition, radar-derived stratiform rain fraction (SF), with
204 categorization into rainfall type described in Powell et al. (2016), was available at
205 the *Mirai*. Here SF was computed as (stratiform rain/total rain) where stratiform
206 rain did not include any contributions from the isolated convective cells and

207 uncertain categories. As a result, the SF values to be shown are lower by ~20% than
 208 those reported in earlier studies (e.g., Xu et al. 2015), but their diurnal trend is
 209 similar if contributions from these other “less-certain” stratiform categories are
 210 included.

211 For the results to be shown, we define the column-integrated diabatic heating
 212 following Yanai et al. (1973) as:

213

$$214 \quad \langle Q_1 \rangle = LP_o + S + \langle Q_r \rangle = \langle Q_{conv} \rangle + \langle Q_r \rangle \quad (1)$$

215

216 where $\langle () \rangle$ is the vertical integral from the top pressure level p_{TOP} to the surface
 217 pressure p_s , Q_1 the diabatic heating, Q_{conv} the convective heating, S the surface
 218 sensible heat flux, P_o the surface precipitation, L the latent heat of vaporization, and
 219 Q_r the net (shortwave + longwave or SW + LW) radiative heating rate. Terms in (1)
 220 have the units of $W m^{-2}$ but for display purposes they are multiplied by the factor
 221 $g/[c_p(p_s - p_{TOP})]$ to present them in units of $K day^{-1}$, where g is the acceleration of
 222 gravity and c_p is the specific heat of dry air at constant pressure.

223 **3. Results**

224 *a. Rainfall characteristics during the DYNAMO SOP*

225 The SOP rainfall time series averaged over each sounding array is shown in Fig. 2
 226 along with the MJO RMM index (Wheeler and Hendon 2004). This index identifies
 227 25 days (highlighted with light green shading) during the SOP as suppressed
 228 (phases 5-8) over the IO. While rainfall was light over the NSA during these
 229 suppressed phases (SP), the MJO active phases (1-3) were characterized by heavy

230 rainfall over both arrays (Gottschalck et al. 2013). Of these 25 suppressed days, 14
231 occurred prior to the October MJO active phase with 11 prior to the November
232 active phase.

233 The associated TRMM rainfall maps for these two periods are shown in Fig. 3.
234 While the October SP was characterized with a single well-established ITCZ band
235 extending across much of the IO south of the equator, convection during the
236 November SP was less organized with a zonally elongated band of convection south
237 of 10°S and scattered convection west of 70°E. Roughly the first half of the
238 November SP also had a degraded sounding network with the *Revelle* being off-site
239 until 10 November (Fig. 2). Since the rainfall maximum during the October SP laid
240 across the SSA, this 14-day October period will be the focus of this study in which 3-
241 h observations from the enhanced sounding network are used to examine the
242 circulation structure and diagnostic fields associated with this ITCZ band of
243 convection.

244 Another perspective on the convection during the SOP can be seen in Fig. 4, which
245 shows a time-latitude plot of rainfall and mid-level vertical motion, both averaged
246 over the longitudes of the enhanced sounding arrays. While rainfall was strongly
247 suppressed over the NSA during the October SP (also seen in Fig. 2), the SSA during
248 this period was characterized with persistent mid-level upward motion and several
249 (at least 5) pulses of heavy rainfall at 3-4-day intervals with peaks on October 2, 6,
250 9, 11, 14. Near the end of the October SP upward vertical motion and rainfall
251 appeared to expand northward from the ITCZ band between 5°-10°S to a more
252 equatorial position (Johnson and Ciesielski 2013; Xu et al. 2015). Furthermore, the

253 time-longitude plot of TRMM rainfall over the SSA (not shown) suggests, at times, a
254 slight westward propagation of rainfall features within the ITCZ band consistent
255 with the weak, but deep, easterly flow over this region (Fig. 5a).

256 *b) Mean flow characteristics of October suppressed period*

257 Using the CSU gridded analysis product, north-south cross sections have been
258 created of the mean circulation and diagnostic fields averaged from 72°-80°E during
259 the October SP (Fig. 5). During this period, ITCZ convection was primarily situated
260 between 5 and 10°S (Fig. 3). Deep easterlies were present in this zonal band (Fig.
261 5a), potentially indicative of vertical momentum transport by deep convection. The
262 other latitudes exhibit a 1st baroclinic mode structure with zonal wind reversals in
263 the vertical, with westerlies (easterlies) underlying strong easterlies (westerlies) to
264 the north and south, respectively, of the ITCZ. Reversals are also observed in the
265 meridional winds (Fig. 5b) resulting in low-level convergence and upper-level
266 divergence peaking near 7°S (Fig. 5c) and a broad region of deep rising motion
267 between the equator and 11°S (Fig. 5d). A shallow meridional return flow from the
268 southern to the northern hemisphere was present near 500 hPa (Fig. 5b). Similar
269 shallow meridional circulations have been observed over the ITCZ in the eastern
270 Pacific and in other monsoon regions (Zhang et al. 2004, Zhang et al. 2008). On
271 either side of the ITCZ, compensating sinking motion was present throughout the
272 troposphere. Unlike idealized zonally symmetric models in which the ITCZ is
273 coincident with converging low-level northerlies and southerlies (Hack et al. 1989,
274 Schubert et al. 1991), here the low-level convergence resulted from a rapid
275 deceleration of the southerlies with a portion of this flow extending beyond the ITCZ

276 northward into the NH (Fig. 5b). The $\partial u/\partial x$ term had no significant contribution to
277 the low-level divergence field in the ITCZ region. The structures depicted here have
278 the general characteristics of a local Hadley circulation with the primary focus of
279 this study being the cross-equatorial cell.

280 The large-scale, upper-level flow during the October SP can be visualized in Fig. 6
281 which shows the 200 hPa divergence and velocity potential field over an extended
282 portion of the Eastern Hemisphere which includes the IO. Here the velocity
283 potential χ is computed from the ECMWF OA divergence field δ shown in Fig. 6a
284 using the relationship $\nabla^2 \chi = \delta$. The minimum in χ over the Indonesian/South
285 China Sea region corresponds to a broad area of convectively disturbed weather and
286 upper-level divergence. This pattern is distinct from the continental-scale Asian
287 summer monsoon mode observed by Krishnamurti and Kishtawal (2000) which had
288 a strong diurnal signal centered over Southern India. In Fig. 6b the ITCZ region
289 between 5° and 10°S is characterized as a trough of lower χ values. Divergent flow,
290 which is perpendicular to isolines of χ , was present within the ITCZ as a region of
291 upper-level outflow. In addition, divergent flow associated with convection over
292 Indonesia contributed to the strong upper-level easterlies seen in Fig. 5a over the
293 NSA. While zonal winds contributed little to the low-level divergence pattern over
294 the ITCZ (Fig. 5c), at 200 hPa they account for a significant fraction (> 50%) of the
295 convergence observed over the NSA as surmised from the χ pattern over this region
296 (Fig. 6b). Therefore, the ITCZ-related local Hadley cell over the IO during this period
297 was not an isolated phenomenon but rather its circulation was superimposed on
298 that of the large-scale east-west flow pattern depicted in Fig. 6.

299 The associated apparent heating Q_1 and apparent drying Q_2 fields (Yanai et al.
300 1973) are shown in Figs. 5e and 5f. The large vertical separation between the peaks
301 in Q_1 and Q_2 is indicative of vigorous deep convection within the ITCZ (Yanai et al.
302 1973). Outside this region tropospheric-deep cooling related to radiative effects
303 and low-level moistening (negative Q_2 maxima) associated with shallow, lightly
304 precipitating convection can be seen. Reasons for the double maximum in vertical
305 motion (Fig. 5d) and the heating field (Fig. 5e) within the ITCZ will be considered
306 later. Finally, potential vorticity (PV) and its companion fields – absolute vorticity
307 and potential temperature θ are shown in Figs. 5g and 5h. Layers of enhanced
308 stability, indicated by a tightening of the vertical θ gradient, result in regions of
309 higher PV such as in the tropopause region (above 200 hPa) and south of 10°S near
310 800 hPa where a signature of the trade-wind inversion layer can be seen (Schubert
311 et al. 1995). Advection of PV by the meridional wind resulted in regions near the
312 equator where the condition for inertial instability was satisfied ($f \cdot PV < 0$, where f
313 is the Coriolis parameter; Stevens and Ciesielski 1986). Also the shaded region of PV
314 in Fig. 5h represents a region in which latent heat released within the ITCZ resulted
315 in a reversal in the meridional PV gradient, which satisfies the necessary condition
316 for combined barotropic - baroclinic instability (Charney and Stern 1962, Eliassen
317 1983). This instability can result in ITCZ breakdown (Nieto Ferreira and Schubert
318 1997, Wang and Magnusdottir 2005) and may offer a possible explanation for the 3-
319 day pulses of the ITCZ convection seen in Fig. 4. Using reanalysis datasets, Duvel
320 (2015) found that reversals in the meridional gradient of PV around 10°S over the
321 IO were the likely cause for instabilities that lead to tropical depression initiation.

322 An alternative explanation for at least some of the pulses in ITCZ rainfall could be
323 the presence of convectively coupled waves (Dias and Pauluis 2009) since westward
324 propagating equatorial Rossby waves were observed over the IO during this
325 October period (Gottschalck et al. 2013, Fig. 13).

326 *c. Diurnal characteristics of convection and attendant flow during October suppressed*
327 *period*

328 We now leverage the 8/day sampling of observations during the October SP to
329 examine the characteristics of the diurnal cycle. The diurnal cycle of TRMM rainfall
330 was largely out of phase between the NSA and SSA during the October SP (Fig. 7a).
331 Over the SSA, rainfall peaked at 05 LT with broad minimum between 17 and 23 LT.
332 The diurnal rainfall range over the SSA was 4.7 mm/day or about 50% of period
333 mean rate of 9.7 mm/day. In contrast, the NSA was characterized by very light
334 rainfall with a broad morning minimum and weak evening maximum of ~1
335 mm/day.² For context, on the remaining 47 SOP days (a combination of 11
336 convectively suppressed and 36 active days), rainfall over both arrays was similar
337 with an overnight 02 LT maximum and 17-20 LT minimum (Fig. 7b). This is
338 generally consistent with the findings of Sakaeda et al. (2017) who found an early
339 morning rainfall peak (03 LT) over the central IO (their Fig. 1c) based on 11 years of
340 boreal winter TRMM rainfall data.

341 A latitudinal cross-section of rainfall over the longitudes of the sounding arrays
342 (72°-80°E, Fig. 8) for the October SP clearly shows large diurnal changes in rainfall

² The light rain rates over the NSA seen in Fig. 7a should be regarded with some caution as the TRMM product underestimates light rainfall due to the sensitivity of the TRMM sensors (i.e., it undersamples shallow, warm-rain clouds; Xu and Rutledge 2014, Ciesielski et al. 2017).

343 over the ITCZ region with peak rates decreasing from over 20 mm/day in the early
344 morning to around 10 mm/day in the early evening. A small evening rainfall
345 increase over the NSA was confined to within a few degrees of the equator. Using
346 radar data from the two near-equatorial sites, Gan and *Revelle*, a comparison is
347 made between the diurnal cycle of radar rainfall to that from TRMM at these sites
348 for the October SP (Fig. 9). The radar domains for these two sites lie outside the
349 active precipitation area within the SSA. During this light rainfall period, TRMM
350 substantially underestimated (by 30-50% in the mean) radar values at both
351 locations, consistent with the findings from previous studies (Xu and Rutledge 2014,
352 Ciesielski et al. 2017). The rainfall maximum at the *Revelle* occurred at 14LT in both
353 estimates with Gan having a relative maximum at 17 LT and slightly higher peak at
354 02LT. The coexistence of both afternoon and nocturnal peaks in clouds and
355 precipitation in the DYNAMO suppressed regimes was also noted by Ruppert and
356 Johnson (2015) and Johnson and Ciesielski (2017, their Fig. 13b). In the former
357 study it was argued that the afternoon–evening peak in rainfall (14-17 LT) is linked
358 to locally warmer daytime SSTs (Bellenger et al. 2010), higher surface fluxes, and
359 relaxed large-scale subsidence. The present study suggests that diurnal changes in
360 the Hadley circulation (detailed next) were contributing to the afternoon rainfall
361 peak. The nocturnal peak may be related to either propagating tides (Woolnough et
362 al. 2004) and/or diurnal radiative feedback mechanisms, such as those described by
363 GJ77 and Randall et al. (1991). The presence of the nocturnal peak at Gan and its
364 absence at the *Revelle* suggests that regional differences in the thermodynamic state

365 and/or the circulation existed between these sites during the October SP.

366 Examination of these differences is beyond the scope of this study.

367 Associated with these diurnal rainfall variations, Fig. 10 shows the morning (05-
368 08 LT) and evening (17-20 LT) vertical cross-sections of several diagnostic fields.
369 These times were chosen since analysis differences between them were most
370 pronounced and generally correspond to the times of the diurnal rainfall extremes
371 seen in Fig. 7a. Low-level (surface to 850 hPa) convergence in the ITCZ region and
372 low-level divergence over the NSA weakened going from morning to evening (Figs.
373 10a, e). This results in prominent diurnal pulsing in vertical motion (Figs. 10b, f)
374 with much stronger rising (sinking) motion within the ITCZ (over the NSA) in the
375 morning hours. Over the NSA, strong early-morning subsidence gave way to weak
376 subsidence in the evening hours and even slight upward motion, most notably
377 between the equator and 2°N consistent with evening rainfall increase seen in Figs.
378 8 and 9. The diurnal amplitude of vertical motion over the NSA was ~1.0 hPa/hr,
379 which is about half that observed in the trade wind environment during BOMEX
380 (Table 1, Nitta and Esbensen 1974). The corresponding apparent heating fields
381 (Figs. 10c, g) reflect this diurnal pulsing with morning heating rates in the ITCZ
382 region being nearly double those in the evening. A notable difference in the
383 apparent drying fields (Figs. 10d, h) is the deeper moistening signature in the
384 evening hours over the NSA consistent with the relaxed subsidence during this time
385 and reflecting the moistening effects associated with daytime growth of the cumulus
386 cloud field (Ruppert and Johnson 2015). This moistening is important in the
387 transition from shallow-to-deep convective leading into the MJO convective phase

388 (Johnson et al. 2015, Xu and Rutledge 2016). In summary, these analyses depict a
389 diurnally pulsing Hadley circulation which ran stronger in the early morning hours
390 resulting in peak rainfall in the ITCZ region during this time. This diurnal cycle is
391 consistent with previous findings (GJ77; Hendon and Woodberry 1993; Deser and
392 Smith 1998). In addition, the daytime reduction in subsidence over the NSA within
393 the subsiding branch of the cross-equatorial Hadley cell allowed shallow convection
394 and associated moistening to deepen during the pre-onset stage of the MJO.

395 Figure 11 provides another perspective on the north-south out-of-phase
396 relationship in the low-level divergence and deep-layer (850-200 hPa) vertical
397 motion and their diurnal changes during the October SP. Low-level convergence
398 peaked in the ITCZ near 7°S at 05 LT, while low-level divergence peaked over the
399 NSA a few hours on either side of this time (Fig. 11a). As the low-level ITCZ
400 convergence weakened going into the evening hours, low-level divergence over NSA
401 weakened in concert. Tied to these low-level divergence changes through mass-
402 continuity considerations, upward vertical motion peaked in the ITCZ in the early
403 morning hours with a maximum in compensating subsidence over the NSA near this
404 time (Fig. 11b). Likewise, the minimum in upward motion in the ITCZ region from
405 17-23LT, which is consistent with the diurnal timing of vertical motion during the
406 convectively active periods in TOGA COARE (Sui et al. 1997; see Table 1), coincided
407 with the period of weakest subsidence over the NSA

408 *d. Longer-term context for October SP*

409 As noted earlier, Zhang and Sodowsky (2016) identified 205 ITCZ events lasting
410 2 days or longer over the IO region (60° - 90°E) using TRMM rainfall products from

411 1998-2013. Using the TRMM rainfall record for this same period, we examine
412 whether convective conditions similar to the October SP were present in other years
413 by averaging rainfall over the sounding array areas. Since the SSA to NSA ratio of 1-
414 2-1 filtered daily rainfall was greater than 4 for each day during the October SP
415 indicating persistent heavier rainfall over the SSA (Fig. 2), we examine the diurnal
416 cycle of rainfall on all days in which this threshold ratio was exceeded for six or
417 more consecutive days over either of the arrays. Using these criteria, we identified
418 19 (95) cases with heavier rainfall over the NSA (SSA) with average length of these
419 cases being 7.8 (8.8) days for the NSA (SSA). Considering the number of cases in
420 each region and their average length, this translates into an occurrence rate for
421 these conditions of 9.3 days per year (or 2.5% of days) over the NSA and 52.3 days
422 per year (or 14.3% of days) over the SSA. Over the array with heavier rainfall, its
423 diurnal cycle (not shown) is remarkably consistent to that seen in Fig. 7a with a
424 similar diurnal amplitude (~ 3.5 mm/day) and a maximum (minimum) at 05 LT (20
425 LT). Over the array with suppressed convection, a weak rainfall diurnal cycle
426 (amplitude < 0.4 mm/day) is present and also similar to Fig. 7a with a morning (08-
427 11 LT) minimum and slight peaks at 17 and 02 LT (not shown). While it is unclear
428 from this analysis whether the array with the heavier rainfall contained an ITCZ, the
429 strong diurnal cycle in rainfall in the active region and its out-of-phase relationship
430 to the suppressed region suggests that a diurnally pulsing “Hadley-cell-like”
431 circulation, similar to that observed in the October SP, was present 15-20% of the
432 time over IO in this 16-yr record.

433 **4. Radiative and convective influences on the ITCZ circulation**

434 *a. Observations of deep-layer convective and radiative heating*

435 To assess what mechanisms may be influencing the circulation features during
436 the October SP and their diurnal changes, Fig. 12 examines the diabatic forcing
437 fields, specifically, the diurnal variations in deep-layer convective heating, $\langle Q_{conv} \rangle$
438 and in all-sky column-net radiation, $\langle Q_r \rangle$. Here $\langle Q_{conv} \rangle = \langle Q_1 \rangle - \langle Q_r \rangle$ is computed
439 using the CSU gridded analysis product and CERES Q_r data, where $\langle () \rangle$ is from 850
440 to 200 hPa yielding a deep-layer (DL) average³. $\langle Q_{conv} \rangle$ varied within the ITCZ
441 region from a maximum of ~ 5 K/day near 05 LT to a minimum of 2.7 K/day at 20 LT
442 (Fig. 12a). The 05 LT peak in $\langle Q_{conv} \rangle$ is consistent with the timing of peak rainfall
443 over the SSA (Fig. 7). Over the convectively suppressed NSA, there was a slight
444 uptick in $\langle Q_{conv} \rangle$ after 11 LT. This increase, which maximized at ~ 0.5 K/day in the
445 evening hours (17-20LT), is particularly noticeable between the equator and 2°N .
446 North of the NSA, the larger mid-day increase in $\langle Q_{conv} \rangle$ was associated with deeper
447 land convection over Sri Lanka and southern India. In comparison, the diurnal
448 amplitude of $\langle Q_r \rangle$ was ~ 2 K/day at all latitudes (Fig. 12b) with enhanced radiative
449 heating due to cloud and moisture effects in the ITCZ region and stronger night-time
450 cooling both north and south of the SSA convectively active zone. Using a simplified
451 zonally symmetric model, Raymond (2000) has argued that differential radiative
452 heating between cloudy and clear regions, such as depicted in Fig. 12c, is sufficient
453 to lead to an instability that results in a cross-hemispheric Hadley circulation.

454 *b. Possible factors influencing diurnal cycle of the ITCZ*

³ Since CERES does not provide Q_r estimates at 850 hPa, the CERES $\langle () \rangle$ was from the surface to 200 hPa. However integration of Q_r from the surface to 200 hPa yields virtually identical results to integration from 850 to 200 hPa, as determined from radiative profiles from Gan Island during DYNAMO (Fig. 10 of Johnson et al. 2015).

455 Determining the detailed impacts of these forcing fields on the circulation would
456 require numerical simulations that are beyond the scope of this study; however, we
457 consider a related but important question: “What processes control the diurnal
458 cycle of vertical motion within the ITCZ circulation (as depicted in Figs. 10b,f and
459 11b)?” In a recent modeling study, Ruppert and Hohenegger (2017) found that the
460 diurnal cycle of overturning motion associated with organized deep convection
461 maintains approximate weak temperature gradient (WTG) balance (Sobel et al.
462 2001). Specifically, they find that on scales up to $O(10^3)$ km (roughly the scale of the
463 sounding arrays), the adjustment of the circulation toward WTG balance through
464 propagating gravity waves occurs rapidly relative to the diurnal cycle. Here, we
465 examine the degree to which WTG balance holds in relation to the daily-mean and
466 diurnal variation of the observed deep-layer vertical motion ω_{obs} during the October
467 SP. GJ77 argued that the diurnal cycle of organized convection is driven by diurnal
468 variations of overturning motion related to differential radiative heating between
469 clear and cloudy areas. This argument, which essentially invokes WTG balance, is
470 tested below.

471 WTG balance takes the form

$$472 \quad \omega \approx Q_1 / \left[\left(\frac{T}{\theta} \right) \frac{\partial \theta}{\partial p} \right]$$

$$473 \quad \omega_{\text{conv}} + \omega_r \approx (Q_{\text{conv}} + Q_r) / \left[\left(\frac{T}{\theta} \right) \frac{\partial \theta}{\partial p} \right] \quad (2)$$

474 where ω_{conv} is the deep-layer (DL) vertical motion due to convection, ω_r is the DL
475 vertical motion due to radiative effects Q_r and the denominator is the DL
476 atmospheric lapse rate. Given that lapse rate over the sounding arrays is nearly a

477 constant in the vertical between 850 and 200 hPa (not shown), we limit our
478 analysis to this layer and assume a DL lapse rate value of -0.054 K/hPa. To
479 determine the DL WTG vertical motion associated with radiative effects, we use
480 CERES $\langle Q_r \rangle$ values.

481 Analysis of ω_r as a function of local time and latitude for the October SP can be
482 seen in Fig 13a. As expected, ω_r shows daytime rising motion and nighttime sinking
483 motion in response to daytime short wave (SW) heating and nighttime longwave
484 (LW) cooling, respectively. Nocturnally enhanced subsidence is evident on either
485 side of the ITCZ with it being somewhat diminished over the NSA in comparison to
486 that observed south of the ITCZ. To emphasize the regional impacts of Q_r on the
487 circulation, Fig. 13b shows ω_r as a deviation from its north-south (i.e. 15°N to 15°S)
488 mean at each local time. This analysis demonstrates that at all times of day the
489 differential radiative warming resulting from the effects of clouds and enhanced
490 moisture in the ITCZ supports the local Hadley circulation, consistent with the
491 arguments of Raymond (2000). Within the ITCZ, this analysis shows increased
492 relative rising motion at midday due to locally enhanced shortwave heating (Fig.
493 12b) with increased relative subsidence over the NSA and south of the ITCZ, where
494 daytime radiative heating is weaker. Noteworthy in this deviation ω_r field is that the
495 largest north-south gradient between the ITCZ and the NSA suppressed region
496 occurred during the daylight hours. This is consistent with the analysis in Fig. 12c
497 which shows the gradient in $\langle Q_r \rangle$ between 7°S and 5°N peaking during the daylight
498 hours. While GJ77 suggested that the radiative gradient between disturbed and clear
499 regions peaks at night, this is clearly not the case during the October SP.

500 To assess how WTG balance holds during the October SP, Table 2 compares
501 daily-mean DL WTG vertical motions to ω_{obs} within the ITCZ (5°-8°S) and the NSA
502 (0°-3°N) regions. Here we include the effect of the horizontal temperature advection
503 (*hta*) term $v \cdot \nabla T$ which when normalized by lapse rate yields ω_{hta} with units of
504 hPa/hr. Indeed from Table 2 we note that compared to the other terms, ω_{hta} is
505 considerably smaller supporting the notion of WTG balance in the daily-mean state.
506 This conclusion is corroborated by the excellent agreement between $\omega_{\text{conv}} + \omega_r$ and
507 ω_{obs} . Furthermore, the magnitude of ω_{conv} within the ITCZ highlights the importance
508 of convection for the overall strength of rising motion in the ascending branch of the
509 Hadley cell.

510 To facilitate an assessment of WTG balance within the diurnal cycle, Fig. 14
511 compares the diurnal variations of the WTG vertical motions with ω_{obs} for the ITCZ
512 and NSA regions. Here the fields are shown as perturbations from their daily-means
513 given in Table 2 while ω_{hta} is not included due to its negligible diurnal amplitude in
514 comparison to the other terms. First considering the NSA region, we note that the
515 reduction in subsidence ω_{obs} from 05 to 11 LT over the NSA correlates well with the
516 decreasing subsidence produced by the ω_r field at this time. However this
517 consistency breaks down over the NSA, particularly between 14 to 23 LT when ω_{obs}
518 and ω_r exhibit disparate trends, suggesting that processes other than radiation are
519 playing a significant role. Over the ITCZ region, diurnal trends in the ω_r and ω_{obs}
520 vertical motion fields are generally congruent. For example, the increase in rising
521 motion from 02 to 08 LT and its reduction of 1.5 hPa/hr from 11 to 20 LT agree well
522 with changes in ω_r over these hours. This correlation breaks down at other times,

523 most notably from 08 to 11 LT, when ω_{obs} shows a weakening upward motion at a
524 time when ω_r through short wave (SW) heating effects suggest a strong opposite
525 trend. A possible explanation for this discrepancy may be the effects of SW heating
526 near cloud top, which would stabilize convection (Randall et al., 1991, Ciesielski et
527 al. 2017) and reduce deep-column upward motion. The decrease in upward motion
528 in ω_{conv} in the same timeframe supports this interpretation. The diurnal changes in
529 ω_{conv} are also congruent with ω_{obs} . Overall the good correspondence within the ITCZ
530 (Fig. 14b) between the diurnal trends in total WTG vertical motion (black curve)
531 and that observed (dashed curved) suggests that the diurnal cycle of overturning
532 circulation is consistent with a rapid adjustment towards WTG balance. This
533 diurnal cycle in circulation is driven both by diurnal changes in radiative heating
534 and convective heating consistent with the findings of Ruppert and Hohenegger
535 (2017), who argue that the circulation in tropical organized convection likely
536 maintains approximate WTG balance.

537 To further explore the diurnal cycle of convection within the ITCZ, Fig. 15 shows
538 the October SP-mean vertical structure of vertical motion and convective heating
539 over the course of a day within the ITCZ (5° - 8° S). In both fields there is a dramatic
540 shift from early morning (02-05 LT) bottom-heavy profiles to daytime (08-17 LT)
541 top-heavy profiles. This daytime shift to top-heavy vertical motion coincided with
542 an increase in convergence around 400 hPa and a divergence increase near 200 hPa
543 (Fig. 10e). GJ77 noted this enhanced daytime mid-level convergence in the
544 convective region and attributed it to diurnal changes in the mid-level horizontal
545 pressure gradient related to SW heating in the upper clouds. The evolution of these

546 fields suggests a transition from convective rainfall at night to more stratiform
547 rainfall during the daytime hours. This diurnal evolution was generally similar to
548 findings from previous field campaigns, e.g., the 1978 Winter Monsoon Experiment
549 (Houze et al. 1981; Houze 1982; Johnson and Young 1983).

550 Since the *Mirai* (positioned at 80°E, 8°S) was on the edge of the ITCZ rain band
551 during this period (Fig. 3a), we use its radar data to analyze the rainfall and
552 stratiform fraction for this location (Fig. 16). The peak radar-derived rainfall at
553 05LT and the evening minimum are consistent with the TRMM diurnal variability
554 over the SSA shown in Fig. 7. The dip in radar rainfall at 08LT was not seen in the
555 TRMM rainfall (Fig. 7a), suggesting that sampling issues may be present in this 14-
556 day mean over the limited *Mirai* radar domain. The stratiform fraction (Fig. 16b)
557 had a nighttime minimum, an increase near daybreak, and an early afternoon
558 maximum generally consistent with the evolution of convective heating profiles
559 shown in Fig. 15. Despite the sampling limitations, these radar results corroborate
560 the notion that the ITCZ convection during the October SP underwent a daily
561 evolution from early morning bottom-heavy convective profiles to daytime top-
562 heavy stratiform ones.

563 A contributing factor in the diurnal evolution of ITCZ convection observed in
564 Figs. 15 and 16 is the effects of daytime SW absorption by clouds. For example, Fig.
565 17 shows the cloud radiative forcing (CRF) for longwave (LW), shortwave (SW) and
566 their net (LW + SW) composited by local time of day for rain rates ≥ 10 mm/day
567 based on data from Gan Island during DYNAMO (Ciesielski et al. 2017). This rain
568 rate threshold was chosen as it roughly corresponds to the minimum rate within the

569 ITCZ during the October SP (red curve in Fig. 8). The CRF fields in Fig. 17 are
570 representative of ~18 days satisfying this rain rate threshold. At higher rain rates
571 common within the ITCZ the CRF signatures become more intense as suggested by
572 the CRF versus rain rates composites shown in Ciesielski et al. (2017, their Fig. 6).
573 As seen in Fig. 17c, nighttime hours were characterized by a thin layer of strong LW
574 cooling near 200 hPa with LW heating at low levels. In contrast, daytime conditions
575 show a strong upper-level heating peak slightly below 200 hPa due to SW CRF
576 effects. As noted in Feng et al. 2014, these upper-level peaks in LW cooling and SW
577 heating may in reality occur at a higher altitude due to under-sampling of high
578 clouds and cirrus in the CombRet product. Nevertheless, the localized maximum in
579 radiative heating at midday over the ITCZ region apparent in Fig. 12b is focused in
580 upper levels. At nighttime the prevalence of deep clouds in the ITCZ leads to locally
581 enhanced LW cooling from cloud tops, and warming in the lower-mid troposphere.

582 The finding that the rising branch of Hadley circulation adjusted rapidly towards
583 WTG balance throughout the diurnal cycle provides a basis of support for the
584 general hypothesis of GJ77 that diurnally varying differential radiation may directly
585 drive circulation changes. While this important premise of GJ77 appears consistent
586 with our analyses, other aspects of their argument appear deficient. For example,
587 their notion that the radiative diurnal cycle is larger in the suppressed environment
588 relative to regions of disturbed weather is not the case for the October SP. Figures
589 13b, 14 and 17 reveal that daytime SW heating in the ITCZ region resulted in a
590 larger radiative diurnal amplitude in convective regions (2.1 K/day) relative to
591 areas of suppressed convection (e.g., the NSA; 1.8 K/day). Furthermore, GJ77

592 hypothesized that an enhanced *nighttime* differential radiative gradient (largely due
593 to nighttime LW cooling in suppressed regions) impacts the convective region
594 through mass continuity. On the other hand, while a differential radiative heating
595 gradient that promotes a mass circulation into the ITCZ exist throughout the course
596 of the day, its amplitude is greatest during daylight hours (Fig. 12c), suggesting that
597 the strong CRF at upper levels (Fig. 17b) is stabilizing the lapse rate so as to inhibit
598 deep convection at that time (Kraus 1963; Randall et al. 1991; Xu and Randall 1995).

599 While the precise reasons for the transition to daytime stratiform convection
600 within the ITCZ are unclear from our analysis, the rapid adjustment of the
601 circulation towards WTG balance in this region (Fig. 14b) suggests that the top-
602 heavy SW-CRF assists the daytime transition to a more top-heavy upward motion
603 and Q_1 (Fig. 15). Likewise the LW-CRF in the absence of SW effects at night supports
604 a more bottom-heavy circulation and enhanced precipitation. The link between
605 daytime top-heavy vertical motion within the ITCZ and top-heavy shortwave
606 heating was also found in radiative–convective equilibrium (RCE) simulations of the
607 diurnal cycle of circulation and organized convection by Ruppert and Hohenegger
608 (2017). Their simulations additionally suggest that both lapse-rate effects and
609 diurnal changes in the horizontal radiative gradient are important to the nocturnal
610 enhancement of precipitation.

611 **5. Summary and conclusions**

612 During the special observing period (SOP) of the DYNAMO field campaign,
613 conducted over the Indian Ocean (IO) from 1 October to 30 November 2011, two
614 prominent MJO events were captured by a sounding network that consisted of one

615 array north and one array south of the equator, referred to here as the NSA and SSA,
616 respectively. Sites in this network took 4-8 soundings/day during this period. Using
617 this sounding dataset along with satellite observations of winds and thermodynamic
618 variables, an objectively analyzed gridded product was constructed. Though
619 supplemented with ECMWF analyses to describe the larger-scale flow features over
620 the IO basin, the gridded fields within the sounding arrays were largely independent
621 of any model influence. We augment this 3-h gridded product with CERES and
622 CombRet radiative heating estimates (Feng et al. 2014) and observations of rainfall
623 to investigate the diurnal cycle of convection during the suppressed phase (SP) of
624 the October MJO event. While convection was suppressed over the NSA during this
625 14-day period, an ITCZ was present south of the equator and extended across the
626 southern half of the SSA. Given this unique circumstance, the opportunity presents
627 itself to examine the diurnal cycle of the ITCZ in the southern Indian Ocean (within
628 the SSA) and its relationship to a mostly suppressed region adjacent to the ITCZ on
629 the opposite side of the equator (the NSA), as well as determine cross-hemispheric
630 interactions during the preonset phase of the MJO. *The establishment of a sounding*
631 *network during DYNAMO, straddling the ITCZ and with 3-hourly sonde launches, has*
632 *provided the first-ever opportunity to directly observe the diurnal cycle of a local*
633 *oceanic Hadley circulation.*

634 The principal findings of this study are as follows:

- 635 • The circulation over the sounding arrays during the October SP could be
636 characterized as a local Hadley cell embedded within a large-scale east-west
637 flow associated with convection over Indonesia.

- 638 • Strong rising motion was present within the ITCZ region, between 5°-8°S (i.e.
639 over the SSA), with compensating subsidence over the NSA and poleward of
640 the SSA. The rising motion within the ITCZ was associated with strong low-
641 level convergence resulting from a rapid deceleration of the southerly flow
642 with a portion of this flow extending beyond the ITCZ into the NSA.
- 643 • Rainfall within the ITCZ exhibited a prominent diurnal cycle with a peak-to-
644 peak amplitude ~50% of the mean (9.7 mm/day over SSA) and a 05 LT (20
645 LT) maximum (minimum). Over the NSA, light rainfall (mean ~1 mm/day)
646 was largely out of phase with SSA variation showing a broad morning
647 minimum and peak rates from 17-20 LT.
- 648 • Divergent flow and vertical motion in the arrays indicate a prominent diurnal
649 pulsing of the local Hadley cell corresponding with the diurnal cycle of the
650 ITCZ. This diurnal pulsing is manifest in strong rising (sinking) motion over
651 the ITCZ (NSA) in the early morning hours and a notably weaker circulation
652 later in the day. The diurnal changes in the ITCZ circulation, while not in
653 strict weak temperature gradient (WTG) balance, were consistent with a
654 rapid adjustment toward this balance.
- 655 • Consistent with the rainfall pattern, diurnal variations in the diagnosed
656 apparent heating Q_1 field over the SSA showed an early morning maximum
657 with nearly twice the magnitude of the evening minimum. Apparent
658 moistening rates over the NSA deepened vertically in the late-
659 afternoon/evening hours reflecting a relaxed subsidence field during this

660 time and the daytime development of the cumulus cloud field and its
661 associated moistening effects.

- 662 • Vertical motion and Q_1 within the ITCZ exhibited a diurnal evolution from
663 strong early morning (05LT) bottom-heavy (convective) profiles to weaker
664 daytime top-heavy (stratiform) profiles. This convective transition is
665 consistent with observations in prior studies (e.g., Houze et al. 1981; Houze
666 1982) and is likely assisted by enhanced SW absorption near the cloud top.
- 667 • Radiative heating in the ITCZ is characterized by top-heavy daytime
668 shortwave warming which is likely important for suppressing deep
669 convection during the daytime by stabilizing the column (Kraus 1963;
670 Randall et al. 1991; Ruppert and Hohenegger 2017). Yet this warming, which
671 is localized to the ITCZ, also promotes the daytime evolution to a top-heavy
672 circulation, and therefore likely helps to sustain stratiform convection into
673 the afternoon many hours after the peak in deep convection. This finding
674 supports the notion that horizontal gradients in radiation can drive diurnal
675 changes in circulation, as first hypothesized (albeit in a different manner) by
676 Gray and Jacobson (1977).
- 677 • As a secondary effect of the diurnally pulsing Hadley circulation, the daytime
678 reduction of subsidence in the downward northern branch of the Hadley cell
679 may have locally assisted the afternoon evolution from shallow to congestus
680 clouds over the NSA connected with oceanic diurnal warm layers there,
681 which have been linked to moistening of the low to mid-troposphere during
682 the pre-onset stage of the MJO (Bellenger et al. 2010; Ruppert and Johnson

683 2015, 2016).

684 While the above results are representative of the 14-day October SP, a similar
685 but less robust Hadley cell circulation was observed (not shown) during the 11-day
686 November SP when the ITCZ was generally south of the SSA. In the long-term
687 TRMM rainfall record, conditions similar to the October SP with the appearance of a
688 diurnally pulsing Hadley circulation were present 15-20% of the time over the
689 central IO. In addition, a recent study (Zhang and Sodowsky 2016) has shown that
690 55% of MJOs are initiated within 4 days of an ITCZ over the IO, such that the above
691 results are likely applicable, to some degree, to the pre-onset conditions of many
692 MJO events.

693 One of the objectives of this study was to utilize the high-frequency (3-h)
694 DYNAMO observations to examine the role that different processes play in
695 influencing the diurnal characteristics of a local Hadley circulation. Use of these
696 observations with WTG arguments indicates that the diurnal evolution of both
697 radiative and convective heating played an important role in controlling diurnal
698 variations in vertical motion within the ITCZ. In contrast, over the convectively
699 suppressed NSA, a poor correlation between observed and radiatively driven
700 vertical motion, particularly from 14 to 23 LT, suggests that other processes (e.g.,
701 diurnal fluctuations in the low-level cross-equatorial flow, the influence of oceanic
702 diurnal warm layers, and transient gravity wave activity) played a prominent role in
703 affecting conditions within the descending branch of the local Hadley cell. While
704 work is underway to understand the influence of these other processes, more

705 definitive answers must await numerical simulations that can explicitly represent
706 the higher frequency transient aspects of the response to diabatic forcings within
707 the Hadley circulation system (e.g., Silva Dias et al. 1987, Gonzalez et al. 2017).

708 *Acknowledgments* The CERES radiation data were obtained from
709 <http://ceres.larc.nasa.gov/products.php?product=SYN1deg>, the TRMM 3B42
710 rainfall data from <http://mirador.gsfc.nasa.gov/>, the legacy radar products from
711 http://dynamo.fl-ext.ucar.edu/rsmas/dynamo_legacy/, and the CSU V3b gridded
712 analyses from <http://johnson.atmos.colostate.edu/dynamo/products/gridded/>. In
713 addition, we thank Alex Gonzalez, Masaki Katsumata, Paul Hein, Steve Lang, Brian
714 McNoldy and Brenda Dolan for many insightful discussions. Comments and
715 suggestions of three anonymous reviewers have led to many significant
716 improvements in the manuscript. Finally we thank Richard Taft for his help with the
717 figures. This research was supported by the National Oceanic and Atmospheric
718 Administration (NOAA) under grant NA150AR4310177, by the National Aeronautics
719 and Space Administration under grant NNX13AF74G, by the National Science
720 Foundation (NSF) under grant AGS-1360237 and by NSF grant 1524844 to James
721 Ruppert.

722

723

724

725

726

727

728 **References**

729

730 Albright, M.D., D. R. Mock, E. E. Recker, and R. J. Reed, 1981: A diagnostic study of the
731 diurnal rainfall variation in the GATE B-scale area. *J. Atmos. Sci.*, **38**(7), 1429-
732 1445.

733 Bain, C. L., J. De Paz, J. Kramer, G. Magnusdottir, P. Smyth, H. Stern, and C. C. Wang,
734 2011: Detecting the ITCZ in instantaneous satellite data using spatiotemporal
735 statistical modeling: ITCZ climatology in the East Pacific. *J. of Climate*, **24**(1),
736 216-230.

737

738 Bain, C. L., G. Magnusdottir, P. Smyth, and H. Stern, 2010. Diurnal cycle of the
739 Intertropical Convergence Zone in the east Pacific. *J. of Geophys. Res.: Atmos.*,
740 **115**(D23), D23116.

741

742 Bellenger, H., Y. N. Takayabu, T. Ushiyama, and K. Yoneyama, K., 2010: Role of
743 diurnal warm layers in the diurnal cycle of convection over the tropical
744 Indian Ocean during MISO. *Mon. Wea. Rev.*, **138**(6), 2426-2433.

745

746 Chen, S. S. and Houze, R. A., 1997: Diurnal variation and life-cycle of deep convective
747 systems over the tropical pacific warm pool. *Q.J.R. Meteorol. Soc.*, 123: 357-
748 388. doi:10.1002/qj.49712353806

749

750 Ciesielski, P. E., and Coauthors, 2014a: Quality controlled upper-air sounding
751 dataset for DYNAMO/CINDY/AMIE: Development and corrections. *J. Atmos.*
752 *Oceanic Technol.*, **31**, 741–764 .

753 Ciesielski, P. E, R. H. Johnson, K. Yoneyama, and R. K. Taft, 2014b: Mitigation of Sri
754 Lanka island effects in Colombo sounding data and its impact on DYNAMO
755 analyses. *J. Meteor. Soc. of Japan*, **92**, 385-405.

756 Ciesielski, P. E., R. H. Johnson, X. Jiang, Y. Zhang, and S. Xie, 2017: Relationships
757 between radiation, clouds, and convection during DYNAMO. *J. Geophys. Res.*
758 *Atmos.*, **122**, 2529-2548.

759 Charney J. G., and M. E. Stern, 1962: On the stability of internal baroclinic jets in a
760 rotating atmosphere. *J. Atmos. Sci.*, **19**, 159–172.

761 Deser, C., and C. A. Smith, 1998: Diurnal and semidiurnal variations of the surface
762 wind field over the tropical Pacific Ocean. *J. Climate*, **11**(7), 1730-1748.

763 Dai, A., and C. Deser, 1999: Diurnal and semidiurnal variations in global surface
764 wind and divergence fields. *J. Geophys. Res.: Atmos.*, **104** (D24), 31109-31125.

765 Dias J, and Pauluis O., 2009: Convectively coupled waves propagating along an
766 equatorial ITCZ. *J. Atmos. Sci.*, **66** (8), 2237–2255.

767 Dudhia, J. 1989: Numerical study of convection observed during the winter Monex
768 experiment using a mesoscale two-dimensional model. *J. Atmos. Sci.*, **46**,
769 3077-3107.

770 Duvel, J., 2015: Initiation and intensification of tropical depressions over the
771 southern Indian Ocean: Influence of the MJO. *Mon. Wea. Rev.*, **143**, 2170–
772 2191, doi.org/10.1175/MWR-D-14-00318.1.

773 Eliassen, A. 1983: The Charney-Stern theorem on barotropic-baroclinic instability.
774 *Pure Appl. Geophys.*, **121**, 563-572.

775 Feng, Z., S. A. McFarlane, C. Schumacher, S. Ellis, J. M. Comstock, and N. Bharadwaj
776 2014: Constructing a merged cloud-precipitation radar dataset for tropical
777 convective clouds during the DYNAMO/AMIE experiment at Addu Atoll, *J.*
778 *Atmos. Oceanic Technol.* **31**, 1021- 1042.

779 Gille, S. T., S. G. Llewellyn Smith, and S. M. Lee, 2003: Measuring the sea breeze from
780 QuikSCAT scatterometry. *Geophysical Research Letters*, **30** (3), 1114-1117.

781 Gray, W. M., and R. W. Jacobson Jr, 1977: Diurnal variation of deep cumulus
782 convection. *Mon. Wea. Rev.*, **105**(9), 1171-1188.

783 Gonzalez, A. O., G. Mora Rojas, W. H. Schubert, and R. K. Taft, 2017: Transient aspects
784 of the Hadley circulation forced by an idealized off-equatorial ITCZ. *J. Adv.*
785 *Model. Earth Syst.*, **9**, 668-690, doi:10.1002/2016MS000837.

786 Gottschalck, J., P. E. Roundy, C. J. Schreck III, A. Vintzileos, and C. Zhang, 2013:
787 Large-scale atmospheric and oceanic conditions during the 2011–12
788 DYNAMO field campaign. *Mon. Wea. Rev.*, **141**, 4173-4196.

789 Hack, J. J., W. H. Schubert, D. E. Stevens, and H.-C. Kuo, 1989: Response of the Hadley
790 circulation to convective forcing in the ITCZ. *J. Atmos. Sci.*, **46**, 2957-2973.

791 Hendon, H. H., and K. Woodberry, 1993: The diurnal cycle of tropical convection, *J.*
792 *Geophys. Res.*, *98*(D9), 16623–16637, doi:[10.1029/93JD00525](https://doi.org/10.1029/93JD00525).

793 Herman, M. J., and D. J. Raymond, 2014: WTG cloud modeling with spectral
794 decomposition of heating. *J. Adv. Model. Earth Syst.*, **6**, 1121–1140.

795 Houze, R. A., Jr., 1982: Cloud clusters and large-scale vertical motions in the tropics.
796 *J. Meteor. Soc. Japan*, **60**, 396-410.

797 Houze, R. A., Jr., S. G. Geotis, F. D. Marks, Jr., and A. K. West, 1981: Winter monsoon
798 convection in the vicinity of north Borneo. Part I: Structure and time
799 variation of the clouds and precipitation. *Mon. Wea. Rev.*, **109**, 1595-1614.

800 Huffman, G. J., R. F. Adler, D. T. Bolvin, G. Gu, E. J. Nelkin, K. P. Bowman, E. F. Stocker,
801 and D. B. Wolff, 2007: The TRMM Multisatellite Precipitation Analysis: Quasi-
802 global, multiyear, combined-sensor precipitation estimates at fine scale. *J.*
803 *Hydrometeor*, **8**, 38–55.

804 Johnson, R. H., and G. S. Young, 1983: Heat and moisture budgets of tropical
805 mesoscale anvil clouds. *J. Atmos. Sci.*, **40**, 2138-2147.

806 Johnson, R. H., and X. Lin, 1997: Episodic trade wind regimes over the western
807 Pacific warm pool. *J. Atmos. Sci.*, **54**, 2020–2034.

808 Johnson, R. H., and P. E. Ciesielski, 2013: Structure and properties of Madden–Julian
809 oscillations deduced from DYNAMO sounding arrays. *J. Atmos. Sci.*, **70**, 3157–
810 3179.

811 Johnson, R. H., and P. E. Ciesielski, 2017: Multiscale variability of the atmospheric
812 boundary layer during DYNAMO. To appear in *J. Atmos. Sci.*

813 Johnson, R. H., P. E. Ciesielski, J. H. Ruppert Jr., and M. Katsumata: 2015: Sounding-
814 based thermodynamic budgets for DYNAMO. *J. Atmos. Sci.*, **70**, 598-622.

815 Kerns, B. W., and S. S. Chen, 2014: Equatorial dry air intrusion and related synoptic
816 variability in MJO initiation during DYNAMO. *Mon. Wea. Rev.*, **142**, 1326-
817 1343.

818 Kraus, E. B., 1963: The Diurnal Precipitation Change over the Sea. *J. Atmos. Sci.*, **20**,
819 551–556.

820 Krishnamurti, T.N., and C. M. Kishtawal, 2000. A pronounced continental-scale
821 diurnal mode of the Asian summer monsoon. *Mon. Wea. Rev.*, **128**(2), 462-
822 473.

823 Lin, J.-L., B. E. Mapes, M. Zhang, and M. Newman, 2004: Stratiform precipitation,
824 vertical heating profiles, and the Madden-Julian Oscillation. *J. Atmos. Sci.*, **61**,
825 296-309.

826 Magnusdottir, G., and C. C. Wang, 2008. Intertropical convergence zones during the
827 active season in daily data. *J. Atmos. Sci.*, **65**(7), 2425-2436.

828 Madden, R. A., and P. R. Julian, 1972: Description of global-scale circulation cells in
829 the Tropics with a 40–50 day period. *J. Atmos. Sci.*, **29**, 1109– 1123.

830 Nicholls, M. E., 2015: An investigation of how radiation may cause accelerated rates
831 of tropical cyclogenesis and diurnal cycles of convective activity. *Atmos*,
832 *Chem. Phys.*, **15**, 9003-9029.

833 Nieto Ferreira, R., and W. H. Schubert, 1997: Barotropic aspects of ITCZ breakdown.
834 *J. Atmos. Sci.*, **54**, 251-285.

835 Nitta, T., and Esbensen, S. 1974: Heat and moisture budget analyses using BOMEX

836 data. *Mon. Wea. Rev.*, **102**, 17-28.

837 Nuss, W.A., and D. W. Titley, 1994: Use of multiquadric interpolation for
838 meteorological objective analysis. *Mon. Wea. Rev.*, **122**(7), 1611-1631.

839 Powell, S. W., and R. A. Houze, 2015: The effect of dry large-scale vertical motions on
840 initial MJO convective onset. *J. Geophys. Res. Atmos.*, **120**, 4783–4805

841 Powell, S. W., 2016: Updraft buoyancy within and moistening by cumulonimbi prior
842 to MJO convective onset in a regional model. *J. Atmos. Sci.*, **73**, 2913-2934.

843 Powell, S. W., R. A. Houze, Jr., and S. R. Brodzik, 2016: Rainfall-type categorization of
844 radar echoes using polar coordinate reflectivity data. *J. Atmos. Oceanic
845 Technol.*, **33**, 523-538.

846 Raymond, D. J., 2000: The Hadley circulation as a radiative-convective instability. *J.
847 Atmos. Sci.*, **57**, 1286-1297.

848 Randall, D.A., Harshvardhan, and D. A. Dazlich, 1991: Diurnal variability of the
849 hydrologic cycle in a general circulation model. *J. Atmos. Sci.*, **48**(1), 40-62.

850 Ruppert Jr., J. H., and Johnson, R. H., 2015: Diurnally modulated cumulus moistening
851 in the preonset stage of the Madden–Julian oscillation during DYNAMO. *J.
852 Atmos. Sci.*, **72**, 1622-1647.

853 Ruppert Jr., J. H., and R. H. Johnson, 2016: On the cumulus diurnal cycle over the
854 tropical warm pool. *J. Adv. Model. Earth Syst.*, **08**, 669-690,
855 doi:10.1002/2015MS000610.

856 Ruppert Jr. J. H., 2016: Diurnal timescale feedbacks in the tropical cumulus regime. *J.*

857 *Adv. Model. Earth Syst.*, **08**, 1483-1500, doi:10.1002/2016MS000713.

858 Ruppert Jr, J. H., and C. Hohenegger, 2017: Diurnal circulation adjustment and
859 organized deep convection. Submitted to *J. Climate*.

860 Sakaeda, N., G. Kiladis, and J. Dias, 2017: The diurnal cycle of tropical cloudiness and
861 rainfall associated with the Madden-Julian Oscillation. *J. Climate*, **30**, 3999-
862 4020.

863 Schubert, W. H., P. E. Ciesielski, D. E. Stevens, and H.-C. Kuo, 1991: Potential vorticity
864 modeling of the ITCZ and the Hadley circulation. *J. Atmos. Sci.*, **48**, 1493-1509.

865 Schubert, W. H., P. E. Ciesielski, C. Lu, and R. H. Johnson, 1995: Dynamical
866 adjustment of the trade wind inversion layer. *J. Atmos. Sci.*, **52**, 2941-2952.

867 Silva Dias, P. L., J. P. Bonatti, and V. E. Kousky, 1987. Diurnally forced tropical
868 tropospheric circulation over South America. *Mon. Wea. Rev.*, **115**(8), 1465-
869 1478.

870 Sobel, A. H., J. Nilsson, and L. M. Polvani, 2001. The weak temperature gradient
871 approximation and balanced tropical moisture waves. *J. Atmos. Sci.*, **58**(23),
872 3650-3665.

873 Sodowsky, R., 2016: Cloud and rainfall statistics from the MJO and the ITCZ over the
874 Indian Ocean. 32nd conference on Hurricanes and Tropical Meteorology. San
875 Juan, PR.

876 Stevens, D.E. ,and P.E. Ciesielski, 1986: Inertial instability of horizontally sheared
877 flow away from the equator. *J. Atmos. Sci.*, **43**, 2845-2856.

878 Sui, C.H., K. M. Lau, Y. N. Takayabu, and D. A. Short, 1997: Diurnal variations in
879 tropical oceanic cumulus convection during TOGA COARE. *J. Atmos. Sci.*, **54**(5),
880 639-655.

881 Tao, W. K., S. Lang, J. Simpson, C-H. Sui, B. Ferrier, and M. D. Chou, 1996: Mechanisms
882 of cloud-radiation interaction in the tropics and midlatitudes. *J. Atmos. Sci.*,
883 **53**(18), 2624-2651.

884 Waliser, D.E., and C. Gautier, 1993: A satellite-derived climatology of the ITCZ. *J.*
885 *Climate*, **6**(11), pp.2162-2174.

886 Wang, C.-C. and G. Magnusdottir, 2005: ITCZ breakdown in three-dimensional flows.
887 *J. Atmos. Sci.*, **62**, 1497- 1512.

888 Wielicki, B. A., B. R. Barkstrom, E. F. Harrison, R. B. Lee III, G. L. Smith, and J. E.
889 Cooper, 1996: Clouds and the Earth's Radiant Energy System (CERES): An
890 Earth Observing System experiment. *Bull. Amer. Meteor. Soc.*, **77**, 853–868.

891 Wheeler, M.C., and H. H. Hendon, 2004: An all-season real-time multivariate MJO
892 index: Development of an index for monitoring and prediction. *Mon. Wea.*
893 *Rev.*, **132**(8), 1917-1932.

894 Woolnough, S. J., J. M. Slingo, and B. J. Hoskins, 2004: The diurnal cycle of convection
895 and atmospheric tides in an aquaplanet GCM. *J. Atmos. Sci.*, **61**, 2559-2573.

896 Yanai, M., S. Esbensen, and J.-H. Chu, 1973: Determination of bulk properties of
897 tropical cloud clusters from large-scale heat and moisture budgets. *J. Atmos.*
898 *Sci.*, **30**, 611–627

- 899 Yoneyama, K., C. Zhang, and C. N. Long, 2013: Tracking pulses of the Madden–Julian.
900 *Bull. Amer. Meteor. Soc.*, **94**, 1871-1891.
- 901 Xu, K-M. and Randall, D. A., 1995: Impact of interactive radiative transfer on the
902 macroscopic behavior of cumulus ensembles. Part II: Mechanisms for cloud-
903 radiation interaction. *J. Atmos. Sci.*, **52**, 800-817.
- 904 Xu, W. and S. A. Rutledge, 2014: Convective characteristics of the Madden–Julian
905 oscillation over the central Indian Ocean observed by shipborne radar during
906 DYNAMO. *J. Atmos. Sci.*, **71**, 2859-2877.
- 907 Xu, W., S. A. Rutledge, C. Schumacher, M. Katsumata, 2015: Evolution, properties,
908 and spatial variability of MJO convection near and off the equator during
909 DYNAMO. *J. Atmos. Sci.*, **72**, 4126-4147.
- 910 Xu, W., and S. A. Rutledge, 2016: Time scales of shallow-to-deep convective
911 transition associated with the onset of the Madden-Julian oscillation. *Geo. Res.*
912 *Let.*, **43**, 2880-2888.
- 913 Zhang, C., 2013: The Madden–Julian oscillation: Bridging weather and climate. *Bull.*
914 *Amer. Meteor. Soc.*, **94**, 1849–1870.
- 915 Zhang, C., M. McGauley, and N. A. Bond, 2004: Shallow meridional circulations in the
916 tropical Eastern Pacific. *J. Climate*, **17**, 133-139.
- 917 Zhang, C., M., D. S. Nolan, C. D. Throncroft and H. Nguyen, 2008: Shallow meridional
918 circulations in the tropical atmosphere. *J. Climate*, **21**, 3453-3470.

919 Zhang, C., J. Gottschalck, E. D. Maloney, M. W. Moncrieff, F. Vitart, D. E. Waliser, B.
920 Wang, and M. C. Wheeler, 2013: Cracking the MJO nut. *Geophys. Res. Lett.*, **40**,
921 1223–1230, doi: 10.1002/ grl.50244.

922 Zhang, C. and R. C. Sodowsky, 2016: Large-Scale and Convective Characteristics of
923 the ITCZ and MJO Initiation Over the Indian Ocean. *AGU Fall Meeting Abstract*

924

925

926

927

928

929

930

931

932

933

934

935

Field Program / Study	Location and Weather Regime	Study Duration	Sounding frequency	Mean vertical motion	Vertical motion diurnal cycle
BOMEX Nitta and Esbensen (1977)	Western Atlantic trade- wind	9 days in July 1969	1.5 hr	+2 hPa/h near 800 hPa	~2 hPa/h at 08 LT
GATE Albright et al. (1981)	Eastern Atlantic ITCZ/easterly waves	3 20-day periods in July to Sept. 1974	6 hr	-0.7 hPa/h near 750 hPa	~1.0 hPa/h at 00 LT
ASTEX Ciesielski et al. (2001)	Eastern Atlantic stratoculumus transition zone	14 days in June 1992	3 hr	+2.5 hPa/h near 825 hPa	~0.8 hPa/h at 22 LT
TOGA COARE Sui et al. (1997)	Western Pacific warm pool	97 days within Nov. 1992 to Feb. 1993	6 hr	-2 hPa/hr near 400 hPa	~1.0 hPa/h at 22 LT

938 Table1. Summary of studies which used tropical/subtropical field program
939 sounding datasets to examine the diurnal cycle of diagnosed atmospheric fields over
940 the ocean. Field programs include: BOMEX (Barbados Oceanographic and
941 Meteorological Experiment), GATE (GARP Atlantic Tropical Experiment), ASTEX
942 (Atlantic Stratocumulus Transition EXperiment) and TOGA COARE (Tropical
943 Oceanic Global Atmosphere Coupled-Ocean Atmosphere Response Experiment). The
944 last two columns list various attributes of the vertical motion field (e.g., its mean and
945 diurnal amplitude defined here as the peak to peak difference, the vertical location
946 of peak amplitude and diurnal variation, and the LT of peak anomalous subsidence).
947 Note: for TOGA COARE the diurnal characteristics listed here are for convectively
948 disturbed periods.

949

950

951

952

953

954

955

956

957

958

959

960

961

Region	ω_{hta}	ω_r	ω_{conv}	$\omega_{conv} + \omega_r$	ω_{obs}
NSA	0.02	0.83	-0.47	0.36	0.39
ITCZ	0.06	0.48	-3.15	-2.67	-2.62

962

963 Table 2. Daily-mean values of deep-layer (DL; 850-200 hPa) WTG vertical motions

964 (hPa/hr) averaged over October SP for various terms in thermodynamic equation

965 for the NSA (0°-3°N) and ITCZ (5°-8°S) regions. (left to right) DL vertical motion

966 resulting from: horizontal temperature advection (*hta*), radiation heating (*r*),

967 convection heating (*conv*), sum of convection and radiative heating, and observed.

968 See text for additional details.

969

970

971 **Figure caption list**

972 Fig. 1. Map showing the DYNAMO enhanced sounding network with color coding of
973 dots indicating frequency of soundings during the Special Observing Period
974 (SOP). Note that soundings at *SK* and *BJ* sites were available only for short
975 periods during the SOP.

976 Fig. 2. Time series of 3-day running mean TRMM 3B42 rain rate (mm/day) averaged
977 over the NSA (black) and SSA (red). Light green shading denotes suppressed
978 periods (RMM index from 5 to 8). The focus of this study is on the October
979 suppressed period when ITCZ convection was located over the SSA with
980 suppressed conditions and little rainfall over the NSA. R/V *Revelle* was off-site
981 from 29 October to 10 November. The RMM MJO index is shown along the
982 bottom of the figure.

983 Fig. 3. (top panel) Rainfall map based on TRMM 3B42v7 product for the 14-day period
984 from 1-14 October 2011. (bottom panel) As in top panel except for the 11-day
985 period from 6-16 November 2011. Outline of enhanced sounding arrays is shown
986 in magenta color. The color scale for rainfall (mm/day) is on the right.

987 Fig. 4. Hovmöller plot for daily-averaged TRMM 3B42 rainfall (mm/day with color
988 scale at bottom) and mid-level (400-500 hPa) vertical motion (contoured with
989 interval 5 hPa/hr) averaged over 72°-80°E for the DYNAMO SOP period. Heavy
990 solid line is the zero contour of vertical motion. Latitudinal limits of enhanced
991 sounding arrays are shown with horizontal dashed lines. The October SP is
992 indicated with light gray shading.

993 Fig. 5. ITCZ period-mean (1-14 October 2011) latitudinal cross-section averaged over
994 72°-80°E for (a) zonal wind field, (b) meridional wind field, (c) divergence, (d)
995 vertical p -velocity, (e) apparent heating, (f) apparent drying, (g) absolute vorticity
996 (color) and potential temperature (contours with 5°K increment), and (h) and
997 potential vorticity. In Fig. 5h the shaded region represents the area where the
998 meridional PV gradient is reversed, satisfying the Charney-Stern necessary
999 condition for combined barotropic – baroclinic instability.

1000 Fig. 6. (a) October SP-mean 200 hPa divergence (warm shading shows areas of
1001 divergence, cool shading areas of convergence with contour increment of $5 \times 10^{-6} \text{ s}^{-1}$
1002 and heavy line is zero contour), (b) as in 6a except velocity potential (contours
1003 in units of $10^6 \text{ m}^2 \text{ s}^{-1}$) with divergent wind field (vectors with scale at bottom).

1004 Fig. 7. (a) Diurnal cycle of TRMM 3B42 rainfall over NSA (black) and SSA (red) for
1005 the October suppressed period when the ITCZ was present over the SSA, (b) as in
1006 6a except for remaining 47 days during the DYNAMO SOP. Yellow shading
1007 denotes daylight hours.

1008 Fig. 8. Latitudinal cross section of TRMM 3B42 rainfall averaged over 72°-80°E for 05-
1009 08 LT (blue) and for 17-20 LT (red). Light vertical lines show latitudinal limits
1010 of the enhanced sounding arrays.

1011 Fig. 9. (top) Diurnal cycle of radar rainfall during the October suppressed period for Gan
1012 (black) and *Revelle* (red); (bottom) as in top except from TRMM-3B42 product.
1013 Values in parentheses represent the period means. Yellow shading denotes
1014 daylight hours.

1015 Fig. 10. October SP-mean latitudinal cross-section averaged over 72°-80°E for (a)
1016 divergence at 05-08 LT, (b) omega at 05-08 LT, (c) apparent heating at 05-08LT,
1017 (d) apparent drying at 05-08LT, (e) divergence at 17-20 LT, (f) omega at 17-
1018 20LT, (g) apparent heating at 17-20LT, and (h) apparent drying at 17-20 LT.

1019 Fig. 11. (a) Latitudinal cross section averaged over 72°-80°E showing diurnal variation
1020 of the low-level (surface – 850 hPa) divergence ($\times 10^{-6} \text{ s}^{-1}$ with contour interval of
1021 $0.6 \times 10^{-6} \text{ s}^{-1}$) for October suppressed period, (b) as in 11a except for observed
1022 deep-layer (850-200 hPa) vertical motion (hPa/hr with contour interval of 0.4
1023 hPa/hr). Latitudinal limits of enhanced sounding arrays are shown with light
1024 horizontal lines.

1025 Fig. 12. (a) Latitudinal cross section averaged over 72°-80°E showing diurnal variation of
1026 deep-layer (850-200 hPa) convective heating $\langle Q_{\text{conv}} \rangle$ (Kday^{-1} with contour
1027 interval of 0.5 Kday^{-1}) for October suppressed period, (b) as in 12a except for
1028 deep-layer (surface to 200 hPa) radiative heating (Kday^{-1} with contour interval of
1029 0.3 Kday^{-1}), (c) meridional gradient of $\langle Q_r \rangle$ between sounding arrays shown as
1030 $\langle Q_r \rangle$ at 7°S minus $\langle Q_r \rangle$ at 5°N. Latitudinal limits of enhanced sounding arrays
1031 are shown with light horizontal lines in panels (a) and (b).

1032 Fig. 13. (a) Latitudinal cross section averaged over 72°-80°E showing diurnal variation
1033 deep-layer vertical motion due to radiative effects (hPa/hr with contour interval of
1034 0.4 hPa/hr), (b) as in 13a except shown as a deviation from its north-south (N-S)
1035 mean at each local time (hPa/hr with contour interval of 0.05 hPa/hr). Here the
1036 N-S mean is computed from 15°N to 15°S. Latitudinal limits of enhanced
1037 sounding arrays are shown with light horizontal lines.

1038 Fig. 14. (a) Diurnal variation of perturbation deep-layer (850-200 hPa) vertical motions
1039 (hPa/hr) averaged from 72°-80°E over a portion of NSA (0°-3°N) for the October
1040 suppressed period, and (b) as in Fig. 15 b except averaged over the ITCZ region
1041 (5°-8°S). Observed deep-layer vertical motion (ω_{obs} ; dotted), due to convection
1042 (ω_{conv} ; red), due to radiation (ω_r ; blue), and $\omega_{conv} + \omega_r$ (black). Perturbation of
1043 fields are from mean values listed in Table 2. Note that difference trends in NSA
1044 vertical motions (ω_{obs} and ω_r) between 14 and 20 LT suggest that processes other
1045 than radiation are impacting vertical motion.

1046 Fig. 15. Mean diurnal cycle over the ITCZ (5°-8°S) for the October SP of (a) vertical
1047 motion, (b) mean vertical motion profiles at 02-05 LT (cyan) and at 11-14 LT
1048 (red), (c) as in 15a except for apparent heating Q_1 , and (d) as in 15b except for
1049 mean Q_1 profiles. Fields have been averaged between 72°-80°E.

1050 Fig. 16. Diurnal variation of (a) Mirai radar rainfall (mm/day) and (b) stratiform fraction
1051 (SF in percent) for the October suppressed period. Numbers in parentheses show
1052 period means. Yellow shading denotes daylight hours.

1053 Fig. 17. Cloud radiative forcing fields (top to bottom): longwave (LW), shortwave (SW)
1054 and their net ($Q_r = LW + SW$), respectively, composited by local time for TRMM
1055 rain rates > 10 mm/day based on CombRet radiative estimates from Gan Island
1056 during DYNAMO.

1057

1058

1059

1060

1061

1062

1063

1064

1065

1066

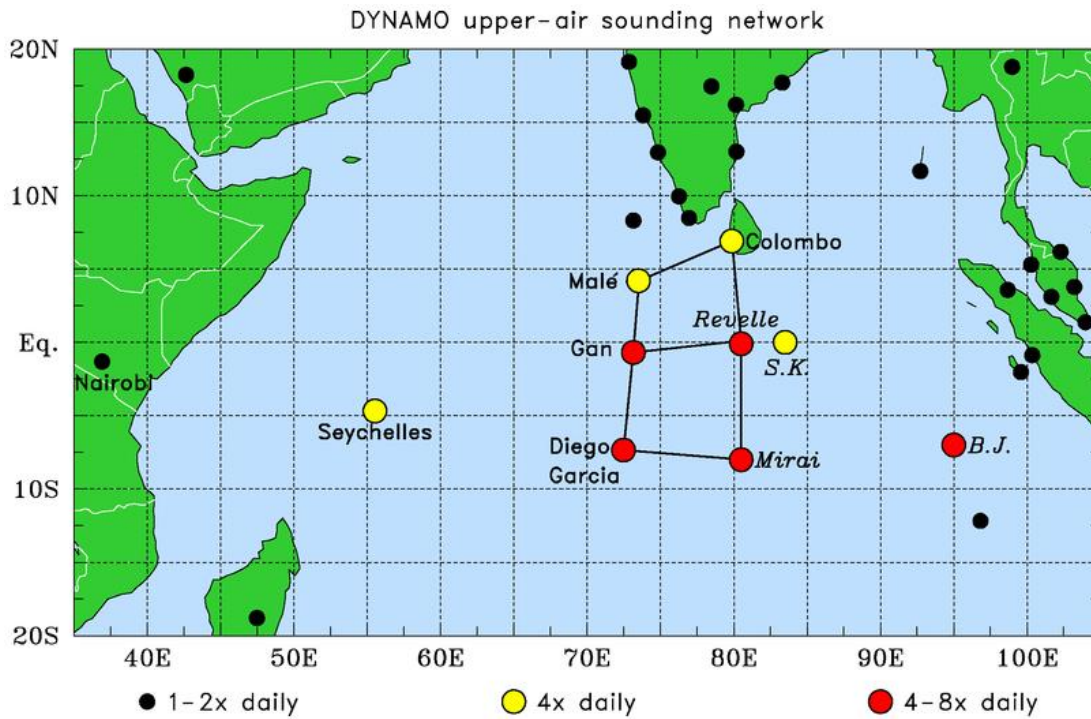
1067

1068

1069

1070

1071



1072

1073

1074

1075

1076

1077

1078

Fig. 1. Map showing the DYNAMO enhanced sounding network with color coding of dots indicating frequency of soundings during the Special Observing Period (SOP). Note that soundings at SK and BJ sites were available only for short periods during the SOP.

1079

1080

1081

1082

1083

1084

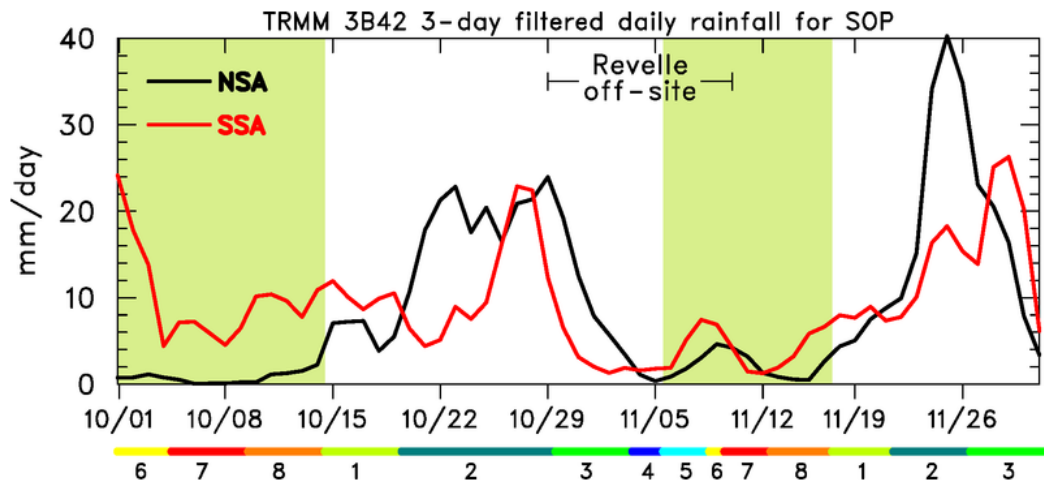
1085

1086

1087

1088

1089



1089

1090 Fig. 2. Time series of 3-day running mean TRMM 3B42 rain rate (mm/day) averaged
1091 over the NSA (black) and SSA (red). Light green shading denotes suppressed periods
1092 (RMM index from 5 to 8). The focus of this study is on the October suppressed period
1093 when ITCZ convection was located over the SSA with suppressed conditions and little
1094 rainfall over the NSA. R/V Revelle was off-site from 29 October to 10 November. The
1095 RMM MJO index is shown along the bottom of the figure.

1096

1097

1098

1099

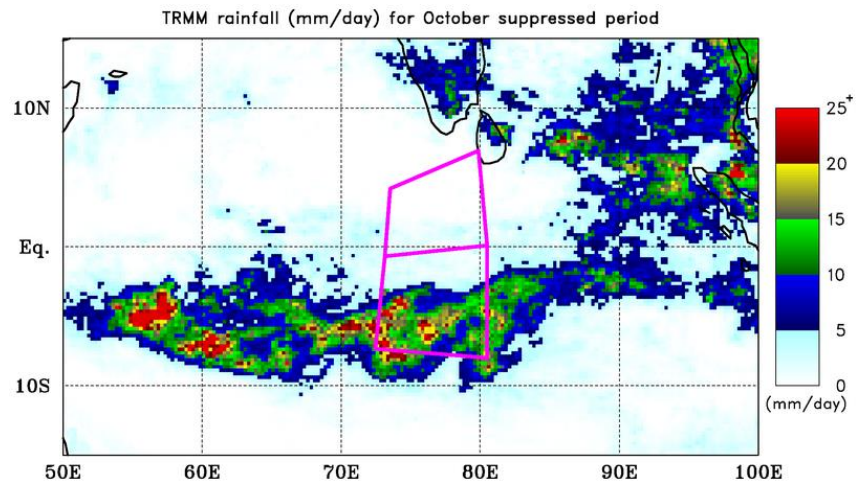
1100

1101

1102

1103

1104



1105

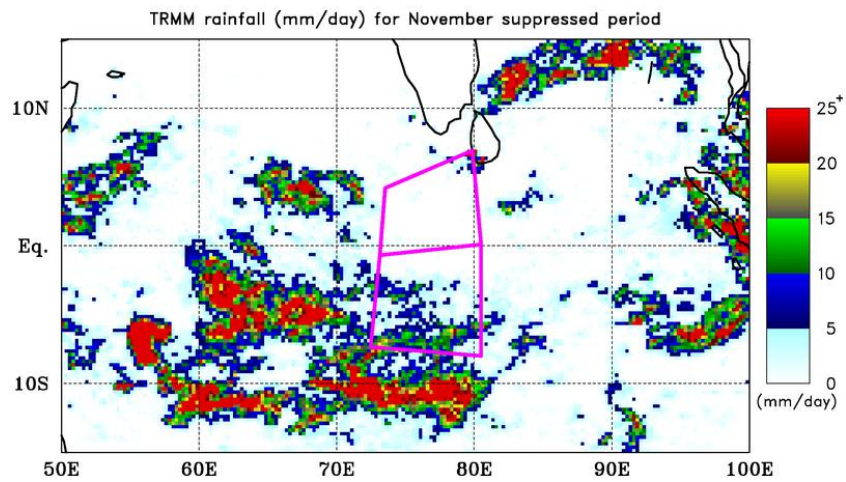
1106

1107

1108

1109

1110



1111 Fig. 3. (top panel) Rainfall map based on TRMM 3B42v7 product for the 14-day period

1112 from 1-14 October 2011. (bottom panel) As in the top panel except for the 11-day period

1113 from 6-16 November 2011. Outline of enhanced sounding arrays is shown in magenta

1114 color. The color scale for rainfall (mm/day) is on the right.

1115

1116

1117

1118

1119

1120

1121

1122

1123

1124

1125

1126

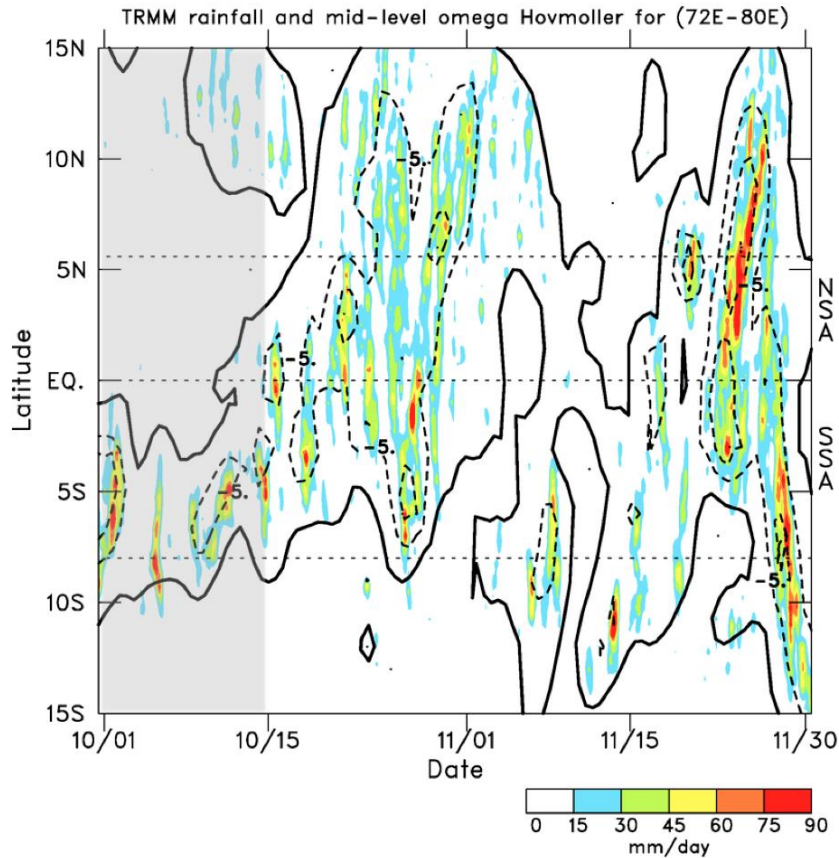
1127

1128

1129

1130

1131



1132

1133

1134

1135

1136

1137

1138

Fig. 4. Hovmöller plot for daily-averaged TRMM 3B42 rainfall (mm/day with color scale at bottom) and mid-level (400-500 hPa) vertical motion (contoured with interval 5 hPa/hr) averaged over 72°-80°E for the DYNAMO SOP period. Heavy solid line is the zero contour of vertical motion. Latitudinal limits of enhanced sounding arrays are shown with horizontal dashed lines. The October SP is indicated with light gray shading.

1139

1140

1141

1142

1143

1144

1145

1146

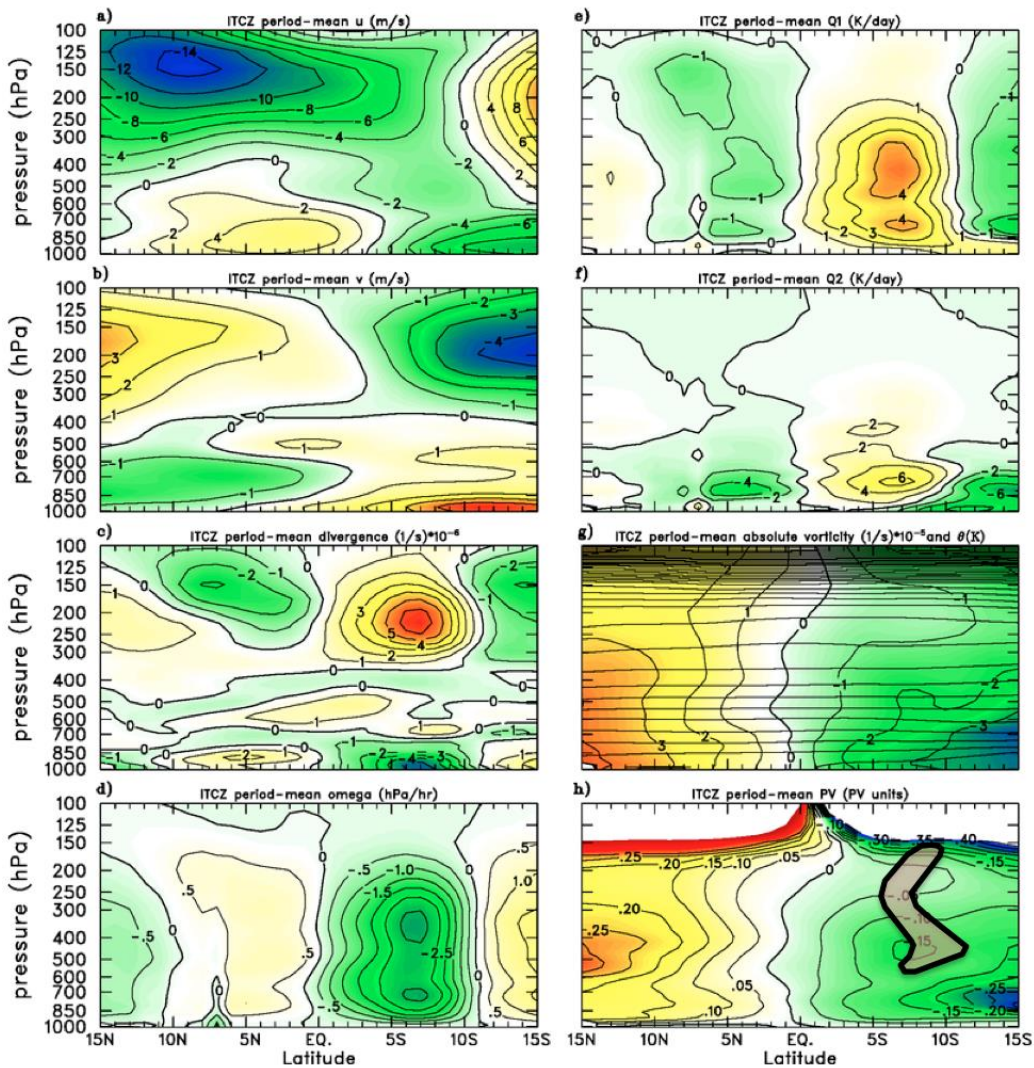
1147

1148

1149

1150

1151



1152

1153

1154

1155

1156

1157

1158

Fig. 5. ITCZ period-mean (1-14 October 2011) latitudinal cross-section averaged over 72°-80°E for (a) zonal wind field, (b) meridional wind field, (c) divergence, (d) vertical p -velocity, (e) apparent heating, (f) apparent drying, (g) absolute vorticity (color) and potential temperature (contours with 5°K increment), and (h) and potential vorticity. In Fig. 5h the shaded region represents the area where the meridional PV gradient is reversed, satisfying the Charney-Stern necessary condition for combined barotropic – baroclinic instability.

1159

1160

1161

1162

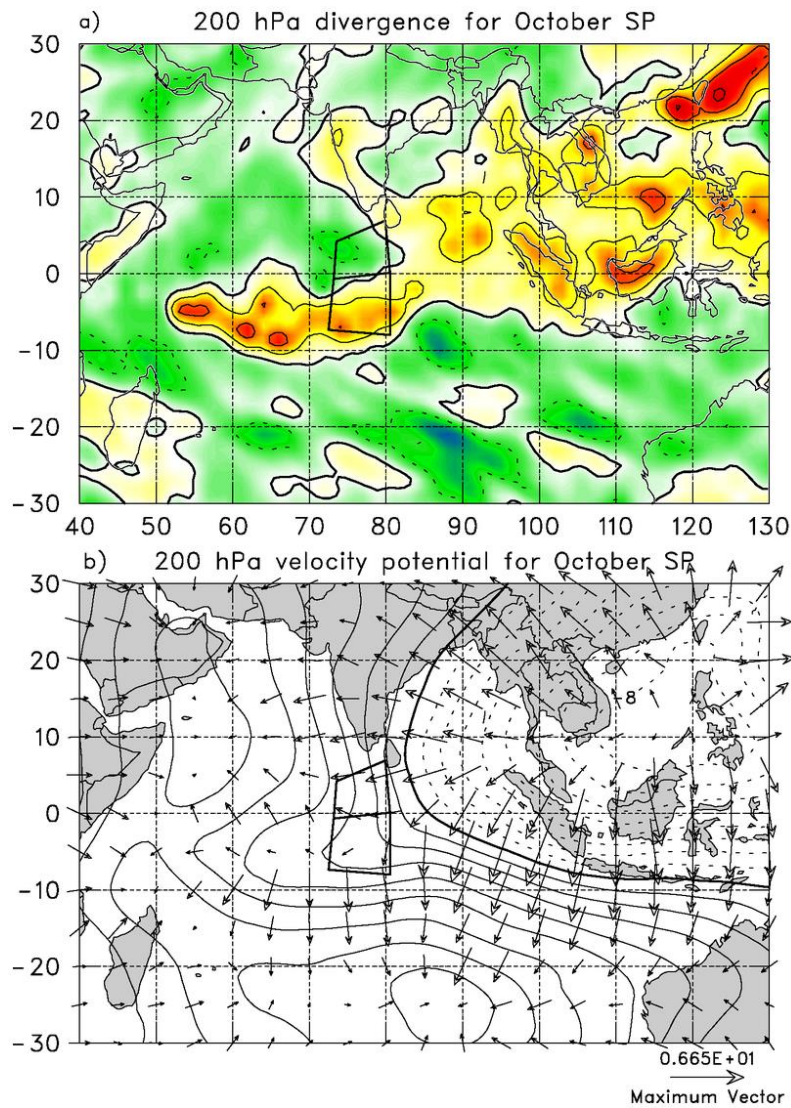
1163

1164

1165

1166

1167



1168

1169

1170

1171

1172

1173

1174 Fig. 6. (a) October SP-mean 200 hPa divergence (warm shading shows areas of
1175 divergence, cool shading areas of convergence with contour increment of $5 \times 10^{-6} \text{ s}^{-1}$ and
1176 heavy line is zero contour), (b) as in 6a except velocity potential (contours in units of
1177 $10^6 \text{ m}^2 \text{ s}^{-1}$) with divergent wind field (vectors with scale at bottom).

1178

1179

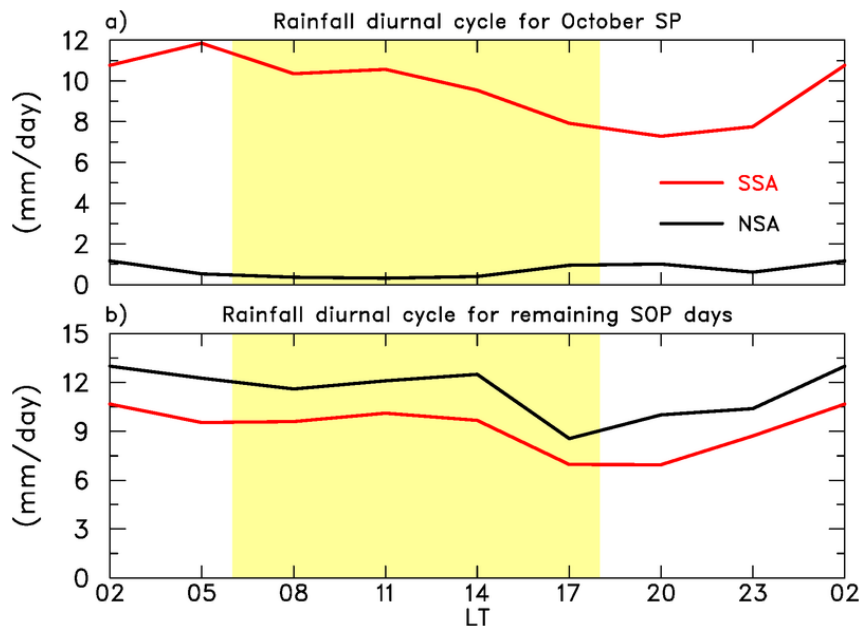
1180

1181

1182

1183

1184



1185

1186

1187

1188

1189

1190

1191

1192 Fig. 7. (a) Diurnal cycle of TRMM 3B42 rainfall over NSA (black) and SSA (red) for

1193 the October suppressed period when the ITCZ was present over the SSA, (b) as in 6a

1194 except for remaining 47 days during the DYNAMO SOP. Yellow shading denotes

1195 daylight hours.

1196

1197

1198

1199

1200

1201

1202

1203

1204

1205

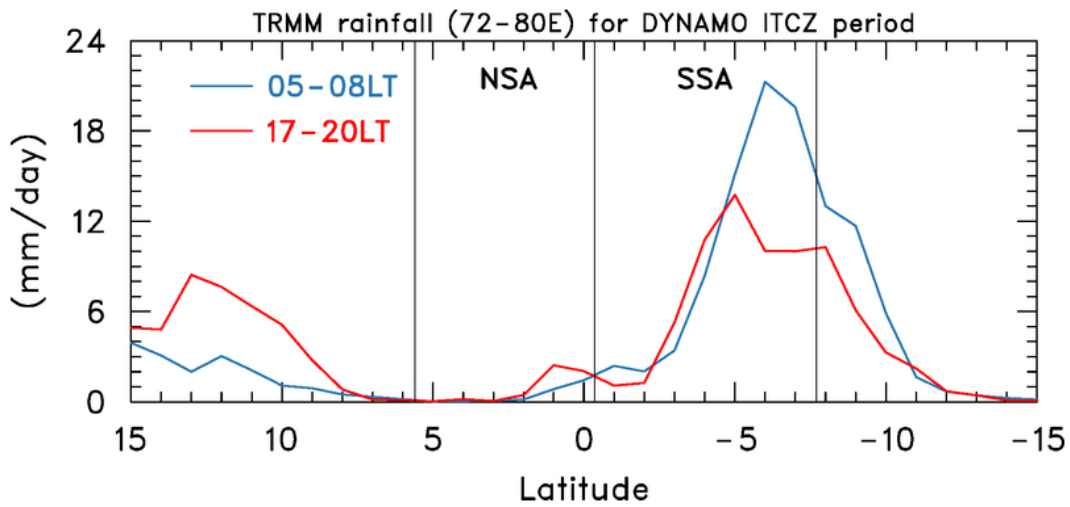
1206

1207

1208

1209

1210



1211 Fig. 8. Latitudinal cross section of TRMM 3B42 rainfall averaged over 72°-80°E for 05-

1212 08 LT (blue) and for 17-20 LT (red). Light vertical lines show latitudinal limits of the

1213 enhanced sounding arrays.

1214

1215

1216

1217

1218

1219

1220

1221

1222

1223

1224

1225

1226

1227

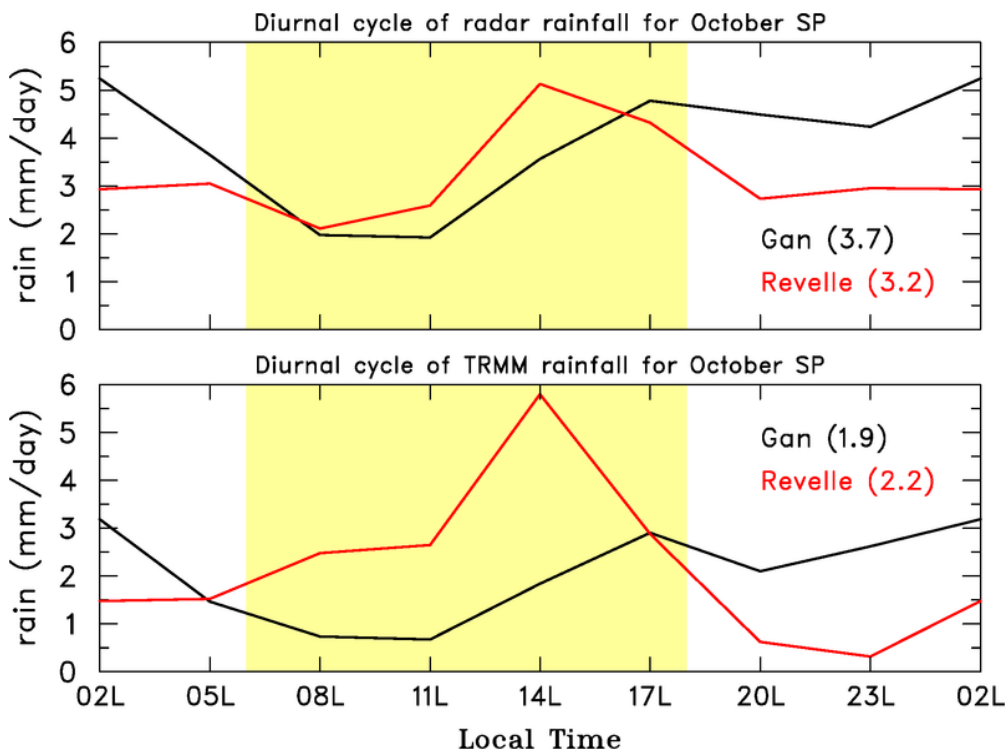
1228

1229

1230

1231

1232



1233 Fig. 9. (top) Diurnal cycle of radar rainfall during the October suppressed period for Gan

1234 (black) and *Revelle* (red); (bottom) as in top except from TRMM-3B42 product. Values

1235 in parentheses represent the period means. Yellow shading denotes daylight hours.

1236

1237

1238

1239

1240

1241

1242

1243

1244

1245

1246

1247

1248

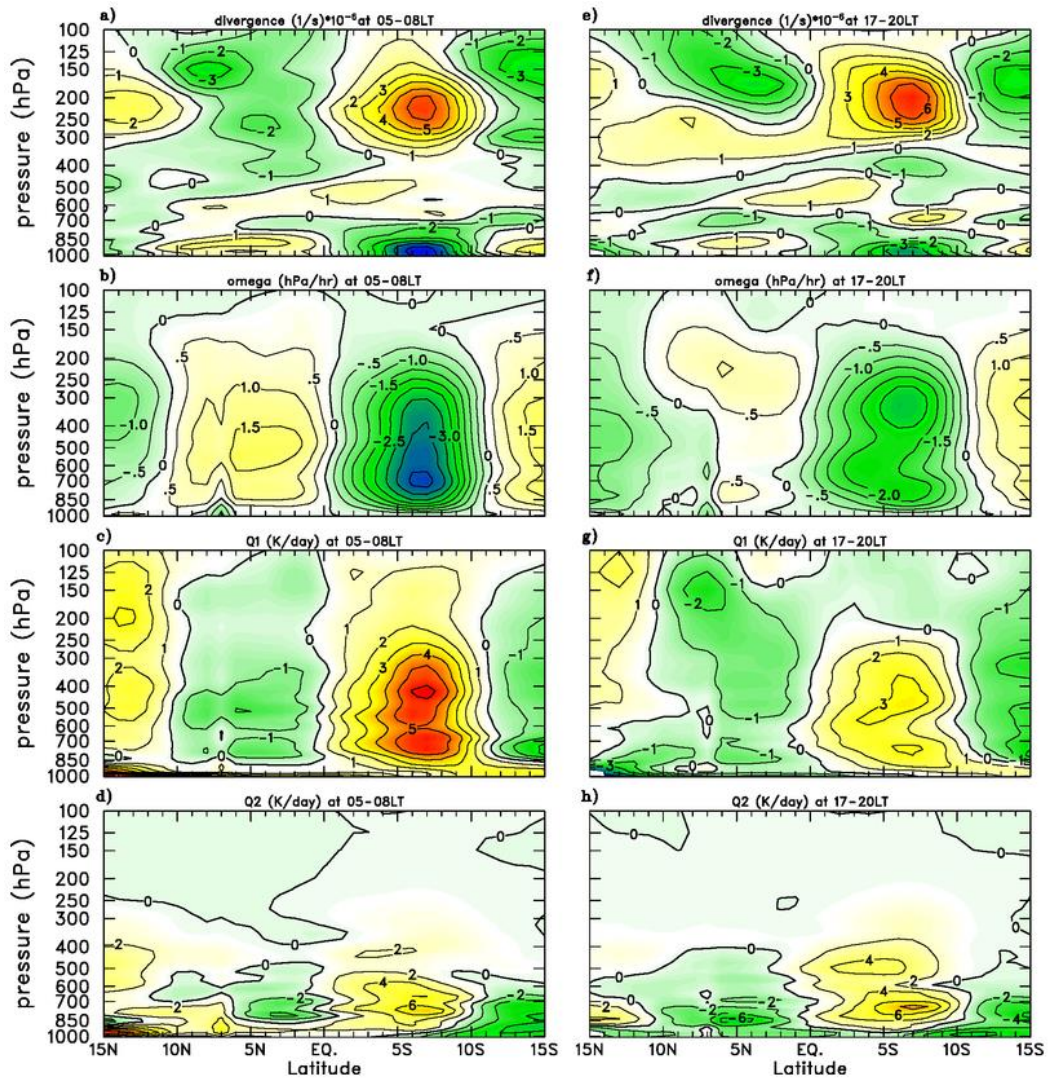
1249

1250

1251

1252

1253



1254 Fig. 10. October SP-mean latitudinal cross-section averaged over 72°-80°E for (a)

1255 divergence at 05-08 LT, (b) omega at 05-08 LT, (c) apparent heating at 05-08LT, (d)

1256 apparent drying at 05-08LT, (e) divergence at 17-20 LT, (f) omega at 17-20LT, (g)

1257 apparent heating at 17-20LT, and (h) apparent drying at 17-20 LT.

1258

1259

1260

1261

1262

1263

1264

1265

1266

1267

1268

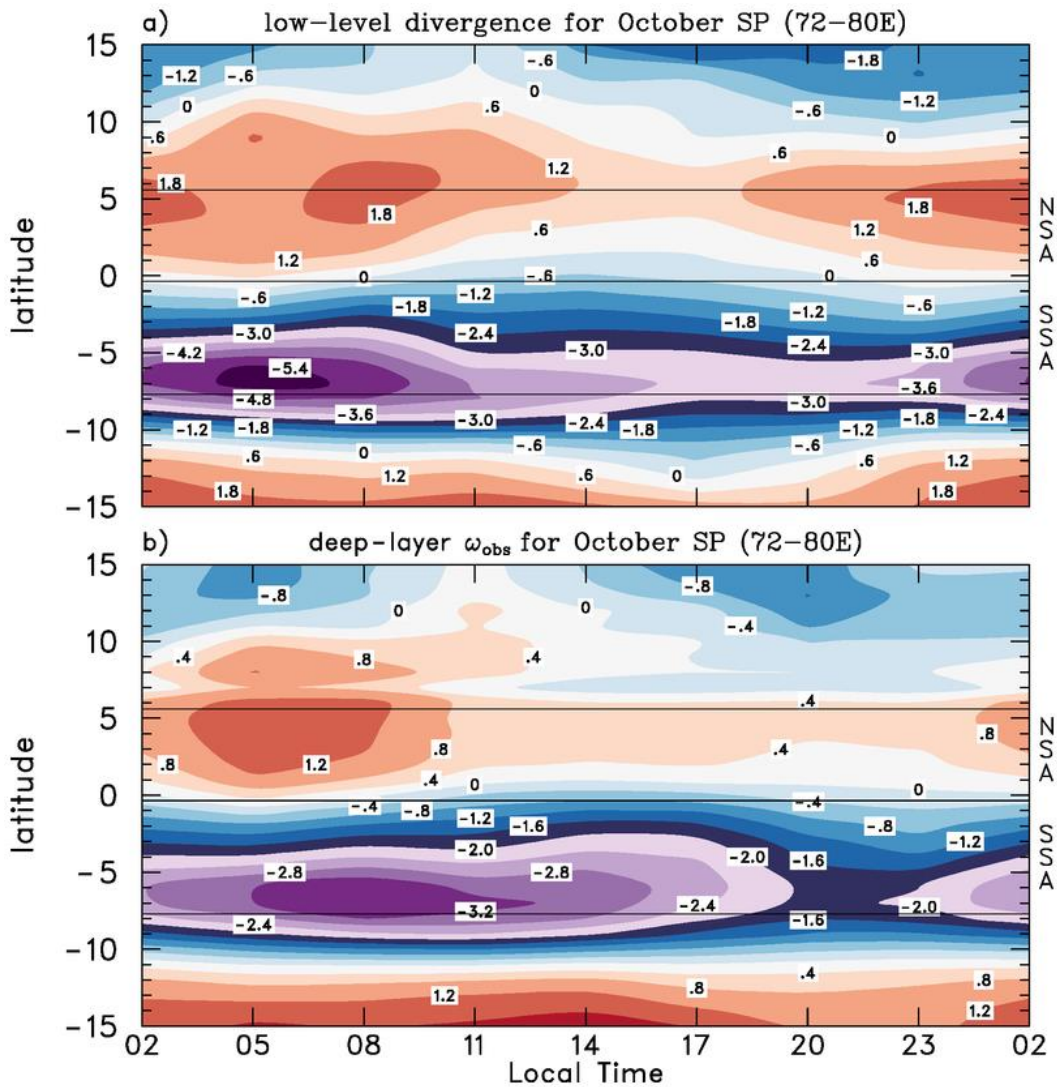
1269

1270

1271

1272

1273



1274 Fig. 11. (a) Latitudinal cross section averaged over 72°-80°E showing diurnal variation
1275 of the low-level (surface – 850 hPa) divergence ($\times 10^{-6} \text{ s}^{-1}$ with contour interval of $0.6 \times$
1276 10^{-6} s^{-1}) for October suppressed period, (b) as in 11a except for observed deep-layer (850-
1277 200 hPa) vertical motion (hPa/hr with contour interval of 0.4 hPa/hr). Latitudinal limits
1278 of enhanced sounding arrays are shown with light horizontal lines.

1279

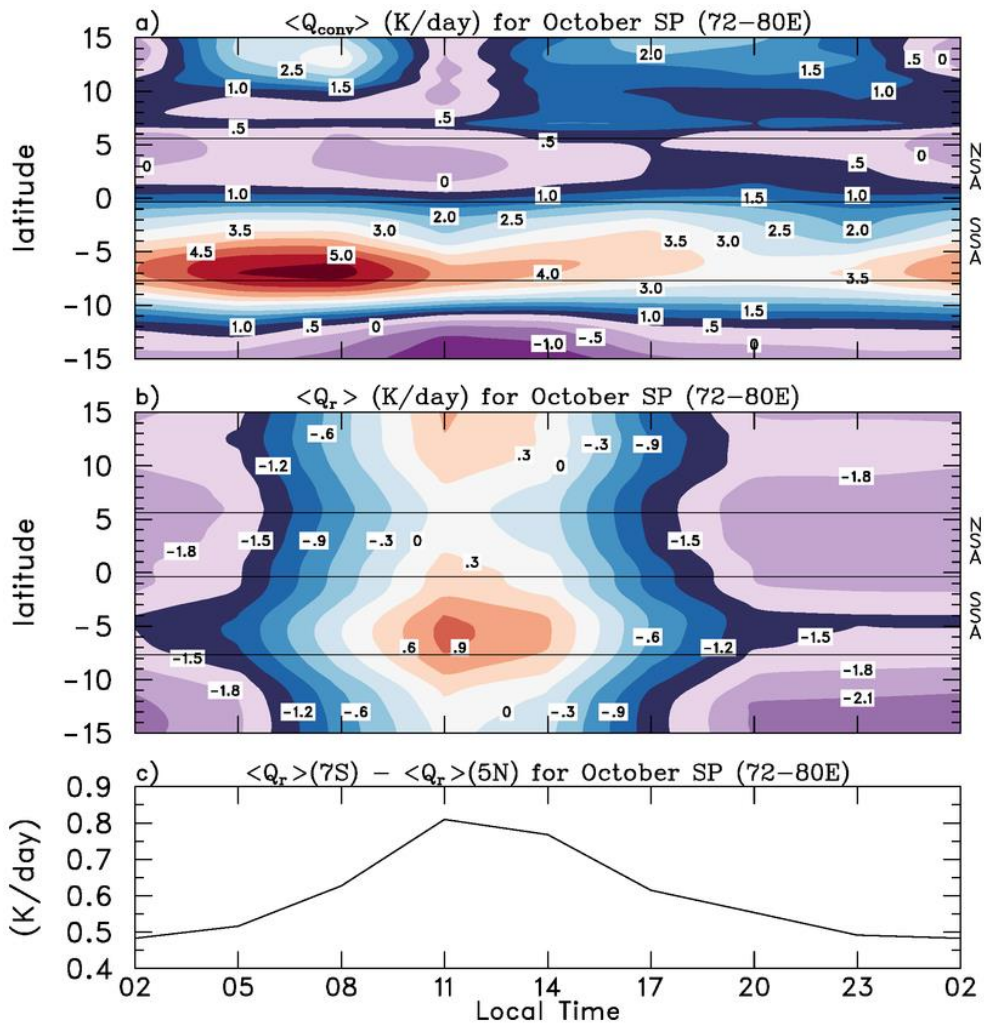
1280

1281

1282

1283

1284



1285

1286

1287

1288

1289

1290

1291

1292 Fig. 12. (a) Latitudinal cross section averaged over 72°-80°E showing diurnal variation of

1293 deep-layer (850-200 hPa) convective heating $\langle Q_{conv} \rangle$ (Kday⁻¹ with contour interval of 0.5

1294 Kday⁻¹) for October suppressed period, (b) as in 12a except for deep-layer (surface to 200

1295 hPa) radiative heating (Kday⁻¹ with contour interval of 0.3 Kday⁻¹), (c) meridional

1296 gradient of $\langle Q_r \rangle$ between sounding arrays shown as $\langle Q_r \rangle$ at 7°S minus $\langle Q_r \rangle$ at 5°N.

1297 Latitudinal limits of enhanced sounding arrays are shown with light horizontal lines in

1298 panels (a) and (b).

1299

1300

1301

1302

1303

1304

1305

1306

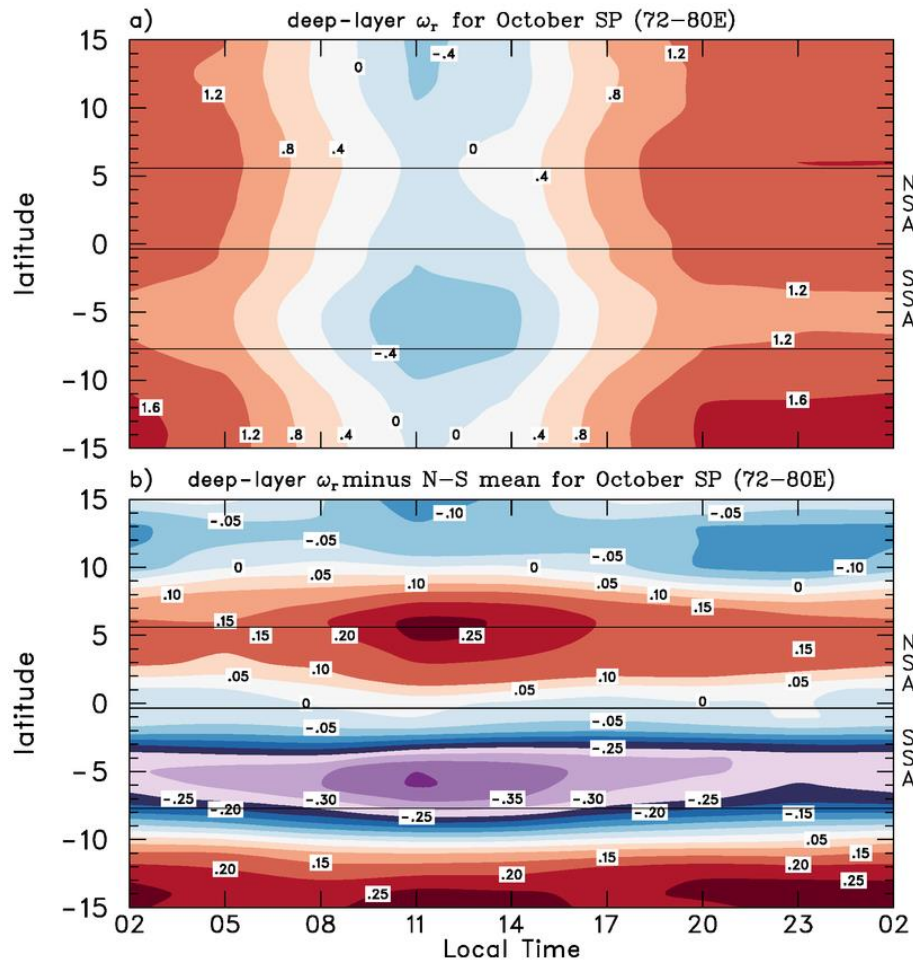
1307

1308

1309

1310

1311



1312 Fig. 13. (a) Latitudinal cross section averaged over 72°-80°E showing diurnal variation

1313 deep-layer vertical motion due to radiative effects (hPa/hr with contour interval of 0.4

1314 hPa/hr), (b) as in 13a except shown as a deviation from its north-south (N-S) mean at

1315 each local time (hPa/hr with contour interval of 0.05 hPa/hr). Here the N-S mean is

1316 computed from 15°N to 15°S. Latitudinal limits of enhanced sounding arrays are shown

1317 with light horizontal lines.

1318

1319

1320

1321

1322

1323

1324

1325

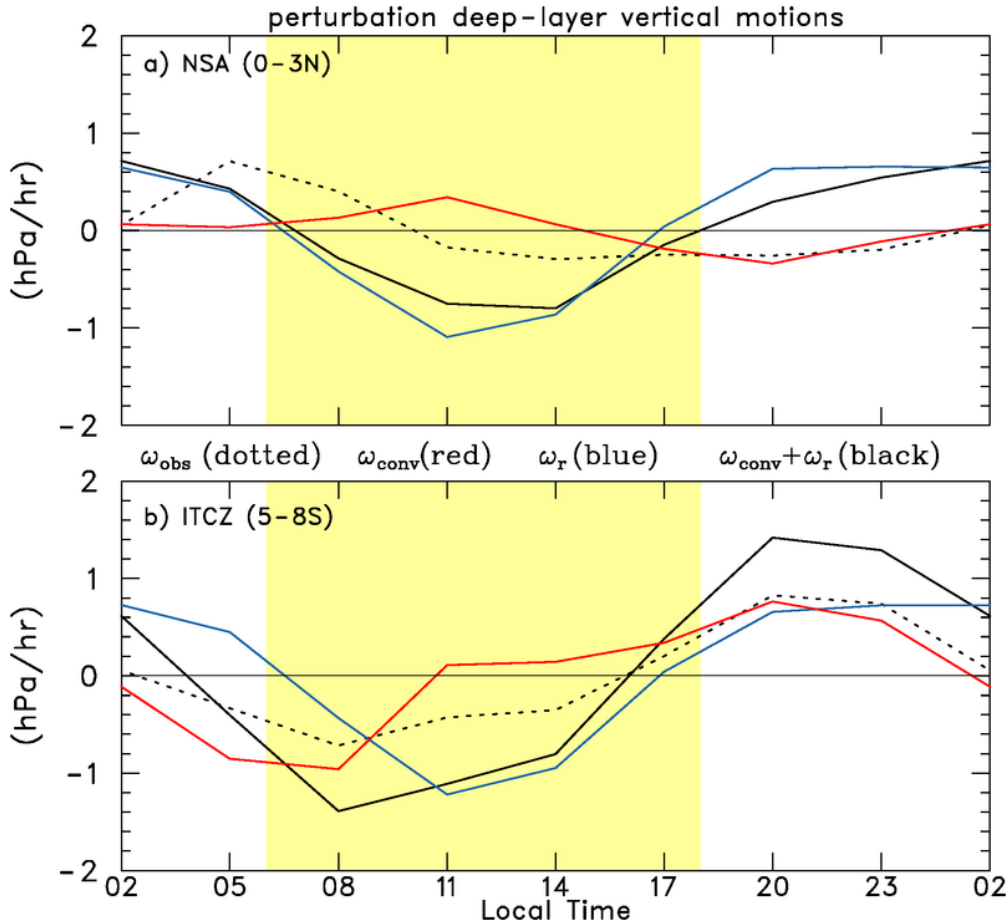
1326

1327

1328

1329

1330



1331 Fig. 14. (a) Diurnal variation of perturbation deep-layer (850-200 hPa) vertical motions
1332 (hPa/hr) averaged from 72°-80°E over a portion of NSA (0°-3°N) for the October
1333 suppressed period, and (b) as in Fig. 15 b except averaged over the ITCZ region (5°-8°S).
1334 Observed deep-layer vertical motion (ω_{obs} ; dotted), due to convection (ω_{conv} ; red), due to
1335 radiation (ω_r ; blue), and $\omega_{conv} + \omega_r$ (black). Perturbation of fields are from mean values
1336 listed in Table 2. Note that difference trends in NSA vertical motions (ω_{obs} and ω_r)
1337 between 14 and 20 LT suggest that processes other than radiation are impacting vertical
1338 motion.

1339

1340

1341

1342

1343

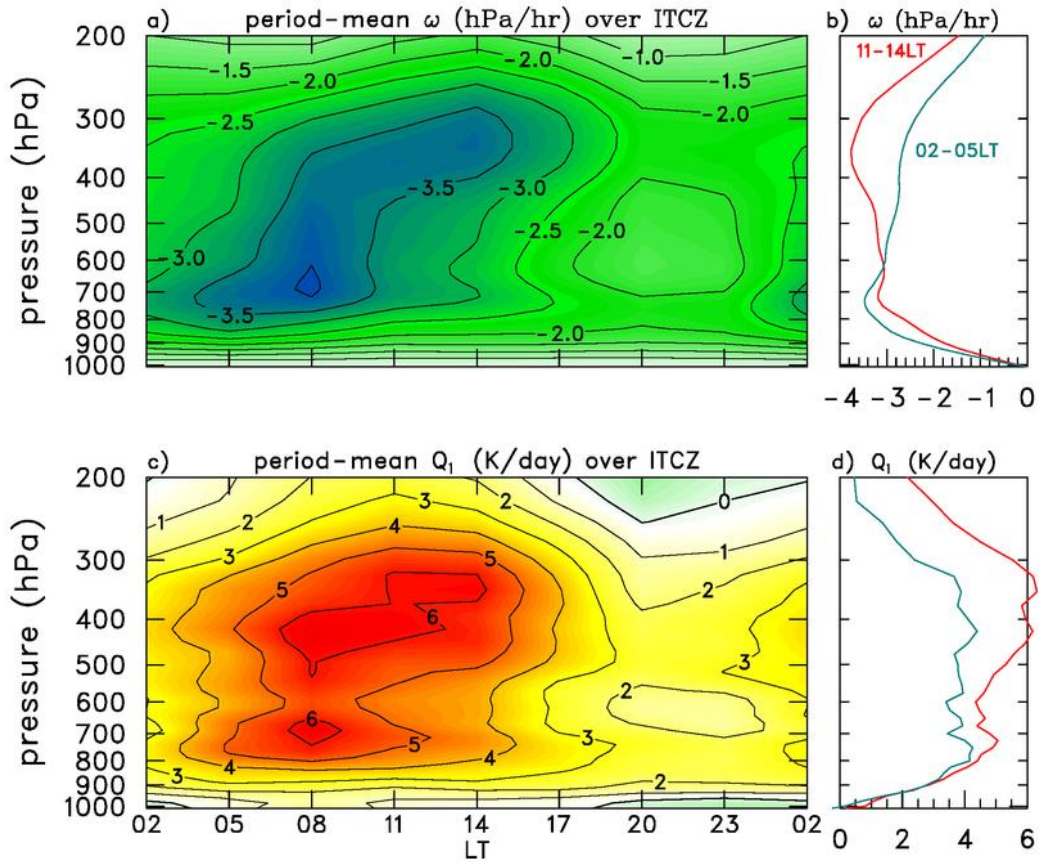
1344

1345

1346

1347

1348



1349

1350

1351

1352

1353

1354 Fig. 15. Mean diurnal cycle over the ITCZ (5°-8°S) for the October SP of (a) vertical

1355 motion, (b) mean vertical motion profiles at 02-05 LT (cyan) and at 11-14 LT (red), (c) as

1356 in 15a except for apparent heating Q_1 , and (d) as in 15b except for mean Q_1 profiles.

1357 Fields have been averaged between 72°-80°E.

1358

1359

1360

1361

1362

1363

1364

1365

1366

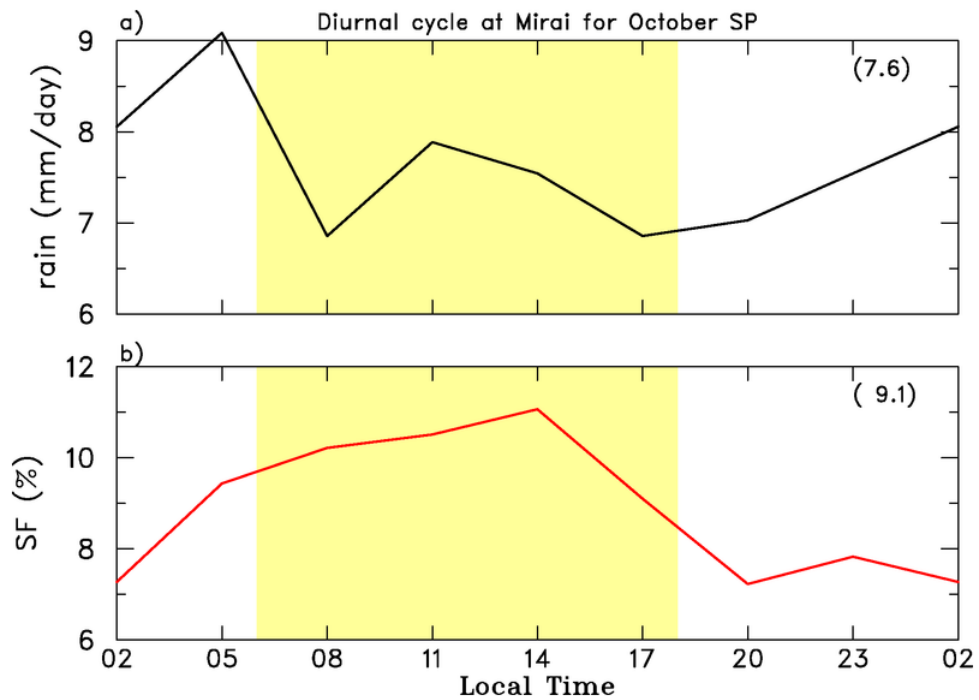
1367

1368

1369

1370

1371



1372 Fig. 16. Diurnal variation of (a) Mirai radar rainfall (mm/day) and (b) stratiform fraction
1373 (SF in percent) for the October suppressed period. Numbers in parentheses show period
1374 means. Yellow shading denotes daylight hours.

1375

1376

1377

1378

1379

1380

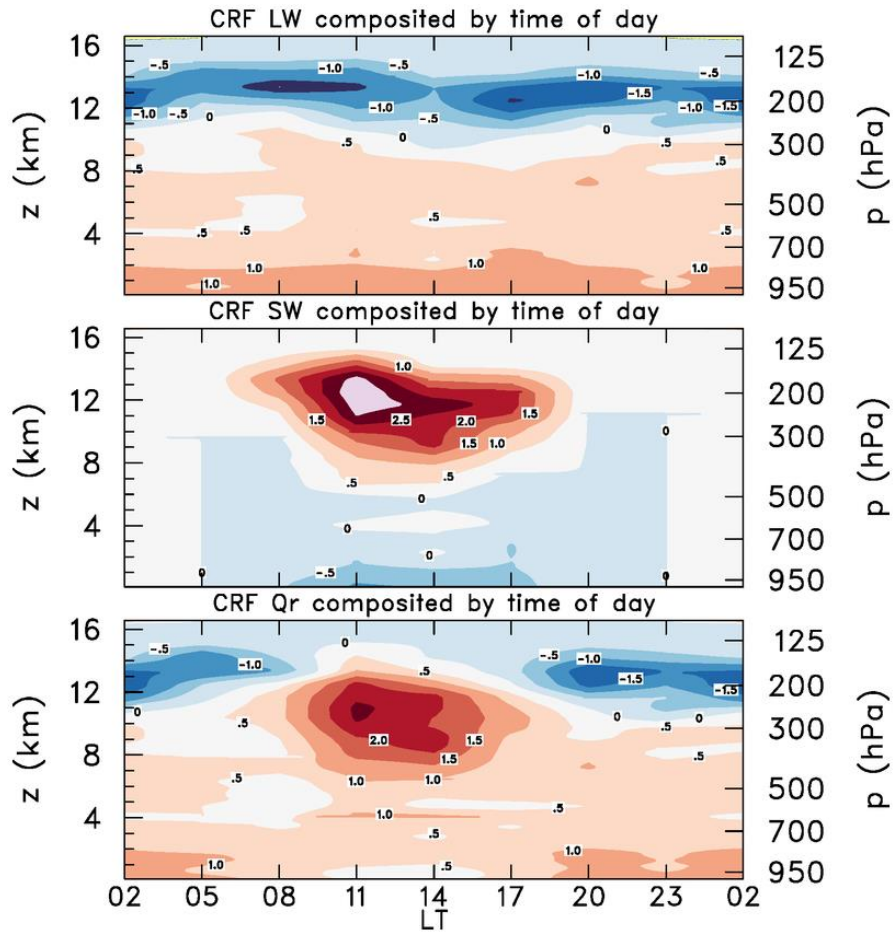
1381

1382

1383

1384

1385



1386

1387

1388

1389

1390

1391

1392

1393 Fig. 17. Cloud radiative forcing fields (top to bottom): longwave (LW), shortwave (SW)

1394 and their net ($Q_r = LW + SW$), respectively, composited by local time for TRMM rain

1395 rates > 10 mm/day based on CombRet radiative estimates from Gan Island during

1396 DYNAMO.

1397

1398

1399